A Frequency Domain Methodology for Quantitative Evaluation of Diffuse Wavefield with Applications to Seismic Imaging

Bo Yang [1,2], Haoran Meng [1,2*], Ning Gu [1,2], Xin Liu [4], Xiaofei Chen [1,3], and Yehuda Ben-Zion[5,6]

[1]Department of Earth and Space Sciences, Southern University of Science and Technology, Shenzhen, 518055, China
[2]Shanghai Sheshan National Geophysical Observatory, Shanghai, 200333, China
[3]Guangdong Provincial Key Laboratory of Geophysical High-resolution Imaging Technology, Southern University of Science and Technology, Shenzhen, 518055, China
[4]Department of Earth Sciences, University of Hong Kong, Hong Kong, China
[5]Department of Earth Sciences, University of Southern California, Los Angeles, California, USA
[6]Statewide California Earthquake Center, Los Angeles, California, USA

Key Points:

- We present an efficient methodology to quantify seismic wavefield diffuseness based on stationarity and randomness in the frequency domain.
- The method avoids waveform normalization and extracts reliable empirical Green's functions from interferometry using diffuse waveforms.
- We validate the method by extracting dispersion curves and Q-values from the 60-second-long diffuse coda of a local M 2.2 earthquake.

Corresponding author: Haoran Meng, `menghr@sustech.edu.cn`

Abstract

Ambient Noise Imaging (ANI) of subsurface structures relies on seismic interferometry of diffuse seismic wavefields. However, the lack of effective methods to quantify and identify highly diffuse waves hampers applications of ANI, particularly in evaluating seismic attenuation and monitoring structural changes with high temporal resolution. Conventional ANI approaches require data normalization, which effectively suppresses the non-diffuse component with large amplitude but also results in significant loss of amplitude and phase information in the continuous seismic records. In this study, we propose a frequency domain method to quantitatively evaluate the degree of diffuseness of seismic wavefields by analyzing their statistical characteristics of modal amplitudes for stationarity and randomness. Tests on synthetic waveform and field nodal records show that the proposed method can effectively distinguish between diffuse and non-diffuse waveforms for either single- or three-component data. As an application, we identify a 60-second-long diffuse coda of a local M 2.2 earthquake recorded by a dense nodal array on the San Jacinto Fault Zone, and successfully extract high-quality dispersion curve and Q-value without performing data normalization. These results are consistent with those obtained by conventional methods that assess the correlation between coherency and the Green's function, and by modeling ballistic waves generated by road traffic. Our proposed method can advance the imaging of subsurface velocity and attenuation structures as well as monitoring temporal changes for scientific studies and engineering applications.

Plain Language Summary

Earthquakes, explosions, and traffic events can generate seismic waves that travel through the Earth. As these direct waves encounter heterogeneous earth interior, they scatter and change direction, leading to more diffusive propagation. Fully diffuse waves can be used to image the subsurface structures. In this study, we develop a reliable and efficient method to measure how diffuse a seismic wavefield is at different frequencies. Tests on synthetic and field data show that the developed method can reliably differentiate between diffuse and non-diffuse waves. This method can improve our ability to use spread out wavefields for imaging and monitoring the Earth's interior.

1 Introduction

Seismic imaging methods have undergone major advances over the past few decades, bifurcating into two primary routes. The first uses ballistic waves generated by seismic sources such as earthquakes, explosions, and traffic events. These ballistic waves provide key data including arrival times, dispersion properties, and amplitude decay as a function of space and time for both body and surface waves (e.g., Nolet, 1977; Taner et al., 1979; Dziewonski & Anderson, 1981; Zhang et al., 2023). Modeling these measurements provides important insights into properties of the Earth interior, including velocity and attenuation structures.

The second route emerged in the early 2000s, leveraging developments in acoustics and seismology that allow reconstructing Green's functions between pairs of receivers through cross-correlations of ambient seismic noise (Lobkis & Weaver, 2001; Weaver & Lobkis, 2001; Shapiro & Campillo, 2004; Paul et al., 2005; Weaver, 2005). As it does not require specific seismic sources, the Ambient Noise Imaging (ANI) method provides an economical and efficient approach that has been widely employed to image seismic velocity, attenuation, and anisotropy from global to local scales (Shapiro et al., 2005; Bensen et al., 2007, 2009; Yao et al., 2006; Yang et al., 2007; Lin et al., 2007; J. Wang et al., 2019; Obermann et al., 2019; Q.-Y. Wang & Yao, 2020; Zhan et al., 2020; Gu et al., 2019, 2022). Additional applications include monitoring temporal changes, geothermal exploration and mineral exploration, further demonstrating its versatility (e.g., Prieto & Beroza, 2008; Brenguier et al., 2014; Obermann et al., 2015; Olivier et al., 2015; Planès et al., 2020; Qiu et al., 2020; X. Xia et al., 2021; Q. Liu et al., 2022; S. Xia et al., 2022).

The theoretical basis of ANI requires diffuse wavefields to derive Green's functions from waveform cross-correlations (Lobkis & Weaver, 2001; Weaver & Lobkis, 2004). A diffuse wavefield within an elastic body of finite size has equal energy across all normal modes and propagates with equal intensity in all directions (Lobkis & Weaver, 2001; Weaver, 1982; Sánchez-Sesma et al., 2008; Snieder et al., 2009; Hennino et al., 2001; Margerin et al., 2009). This implies that a fully diffuse wavefield is stationary and lacks correlations across different frequencies. Such requirements are difficult to satisfy in natural environments with non-random distribution of sources that typically include tectonic, environmental, and anthropogenic sources that are concentrated at specific locations (e.g., Díaz et al., 2017; Inbal et al., 2018; Meng & Ben-Zion, 2018; Fan et al., 2019; Johnson et al., 2020; Diaz et al., 2023; Zhang et al., 2023).

Efforts to tackle this challenge include the utilization of earthquake coda waves and the adoption of waveform normalization techniques. Successful applications have demonstrated the feasibility of reconstructing empirical Green functions (EGFs) from coda waves (Campillo & Paul, 2003; Paul et al., 2005). Additionally, recent studies utilizing correlations of long-period coda waves from large earthquakes (such as $M \geq 7$) have found spurious signals that can illuminate the deep Earth, although the correlations do not necessarily reconstruct the EGFs extracted from ambient noise (e.g. Poli et al., 2017; S. Wang & Tkalčić, 2020; Tkalčić et al., 2020). However, large earthquakes are infrequent and predominantly occur along plate boundaries. Moreover, some studies have shown that their coda waves are complex and lack diffuseness over long periods (Maeda et al., 2006; Sens-Schönfelder et al., 2015; Poli et al., 2017). Consequently, relying solely on these rare events and retrieving their diffuse components for seismic imaging is not practical for mobile and temporary seismic arrays. To leverage ambient noise in ANI while mitigating the influence of earthquakes and other strong sources, normalization has been proved effective for suppressing non-diffuse signals in continuous seismic records. This is done practically by averaging or clipping recorded amplitudes in both the time and frequency domain (Bensen et al., 2007; Schimmel et al., 2011; Seats et al., 2012; Shen et al., 2012; Cheng et al., 2015; Xie et al., 2020). Although the original waveforms are heavily distorted, EGFs with reliable phase can be obtained by stacking the cross-correlation functions from year- or month-long seismic records of seismic arrays in a regional or local scale, respectively (e.g., Shapiro et al., 2005; Yang et al., 2007; Yao & Van Der Hilst, 2009; Ritzwoller et al., 2011; Poli et al., 2012; Lin et al., 2013; Roux et al., 2016; Gu et al., 2019; Mordret et al., 2019).

Alternatively, EGFs with reliable amplitude and phase can be directly extracted by identifying diffuse waveform segments in continuous records, utilizing relatively short waveform lengths without the need for normalization. Multiple approaches have been developed to evaluate the degree of diffuseness of seismic records. Margerin et al. (2009) computed the energy ratio of P- and S-wave using earthquake coda recorded by a dense array, and interpreted the stabilization of the ratio as a signature of diffuseness. Similarly, Sánchez-Sesma et al. (2011) analyzed microtremor wave fields and considered the stabilization of normalized average autocorrelation as an indicator of diffuseness. Another approach involves assessing the constituents of seismic waves at different periods, such as conducting a beamforming analysis to measure directionality. This approach has been applied to multiple $M \geq 7$ earthquakes and has revealed a lack of equipartitioning in the late coda of these large events (Maeda et al., 2006; Sens-Schönfelder et al., 2015; Poli et al., 2017). While these studies provide valuable insights, they either rely on additional simplifying assumptions or necessitate complex analysis of array data. A more straightforward approach, proposed by X. Liu and Ben-Zion (2016), evaluates the degree to which a wave field is diffuse by examining the cross-frequency coherence using a single component record. To further develop this approach, it is important to establish conditions that are both sufficient and necessary indicators of a diffuse wavefield.

In the present paper we present a methodology involving three conditions in the frequency domain that are both sufficient and necessary to establish that a wavefield is diffuse. The method named Evaluation of the Diffuseness of the Wavefield (EDWav) examines the statistics of modal amplitudes that can be efficiently resolved using a dimensionless vector and two dimensionless metrics constructed from the Fourier transforms of waveform segments. To demonstrate the robustness of the method, we analyze seismic waveforms recorded by a dense seismic array centered (Figure 1) on the Clark branch of the San Jacinto Fault Zone (SJFZ) at the Sage Brush Flat (SGB) site near Anza, California (Ben-Zion et al., 2015). The dense seismic array consists of 1108 vertical component 10 Hz nodes and recorded continuously at 500 Hz from May 7 to June 13, 2014 in an area of about 600 m $\times$ 600 m (Figure 1b), with nominal sensor spacing of 10 m normal to the fault and 30 m along-strike (Ben-Zion et al., 2015; Meng et al., 2019). In particular, we quantitatively assess the degree of diffuseness of a local earthquake and discuss the widely used time- and frequency-domain normalization in the ANI preprocessing procedures proposed by Bensen et al. (2007). In addition, we examine the diffuseness of waveform packets dominated by random noise and other signals identified by Meng et al. (2019). Finally, we adopt the EDWav method to separate the ballistic wave and diffuse coda of a local M 2.2 earthquake recorded by the SGB dense array. From the 60-second-long diffuse coda, we successfully reconstruct EGFs with reliable phase and amplitude using seismic interferometry, and extract dispersion curves and Q-values.

2 Methods

2.1 Characteristics of diffuse wavefield in the time domain

A wavefield can be expressed mathematically as the superposition of normal modes (Aki & Richards, 2002). The vector expression in the time domain is given by (Campillo & Paul, 2003)

$$\boldsymbol{\Psi}(\mathbf{r}, t) = \mathrm{Re} \sum_n a_n \mathbf{u}^{(n)}(\mathbf{r}) e^{i\omega_n t}, \tag{1}$$

where a_n are complex modal amplitudes and are independent of direction, $\mathbf{u}^{(n)}(\mathbf{r})$ refers to vector normal mode eigenfunctions, $\mathbf{r}$ is location vector, ω_n is angular frequency corresponding to the n-th mode, t is time, $i^2 = -1$, and Re[$\cdot$] denotes taking the real part

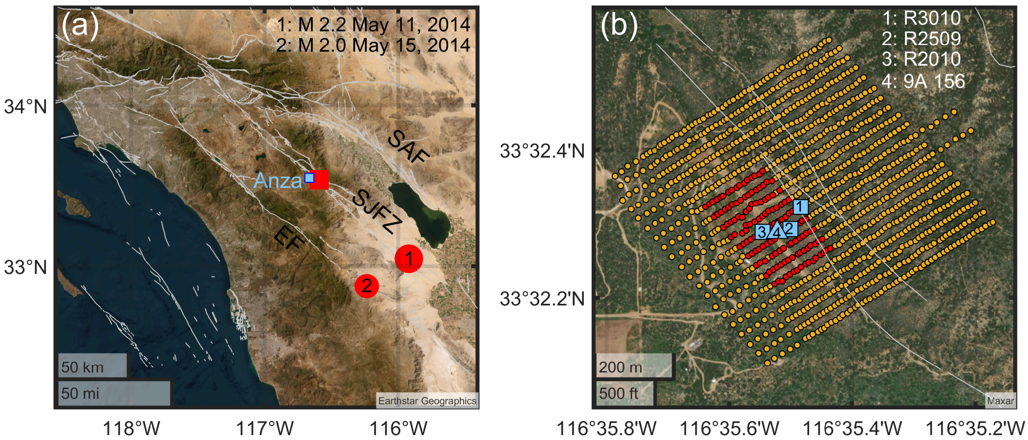

Figure 1. (a) A regional map showing Southern California and the dense array on the San Jacinto fault zone (SJFZ, red square). The red circles denote the epicenters of two local earthquakes with M 2.2 and M 2.0 employed in this study. The M 2.2 occurred on May 11, 2014 at 11:47:09.53 (UTC), located at 33.0458°, −115.9205°, with a depth of 7.73 km. The M 2.0 earthquake occurred on May 15, 2014 at 12:49:21.88 (UTC), located at 32.8740°, −116.2337°, with a depth of 3.49 km (Vernon et al., 2014; White et al., 2019; Ross et al., 2019). (b) Zoom-in view of the dense deployment. Circles denote the 1108 vertical nodes of the dense deployment. The analyzed nodes R3010, R2509, and R2010 are denoted by the squares. The analyzed sub-array is formed by the nodes marked in red. The analyzed 3C node 156 of the 9A network is denoted by a triangle. The backgrounds of (a, b) are satellite images with superposed fault traces.

of a complex function. When considering a single component, we project $\mathbf{\Psi}(\mathbf{r}, t)$ in the direction of the unit vector $\hat{\mathbf{e}}$,

$$\psi(\mathbf{r}, t) = \mathbf{\Psi}(\mathbf{r}, t) \cdot \hat{\mathbf{e}} = \mathrm{Re} \sum_n a_n u^{(n)}(\mathbf{r}) e^{i\omega_n t}, \tag{2}$$

where $\hat{\mathbf{e}}$ could be either vertical or horizontal. In the case of a fully diffuse wavefield, the waveform should exhibit randomness and lack of coherence across different frequencies. The statistics of the modal amplitudes then satisfy (Weaver & Lobkis, 2004)

$$\mathrm{E}[a_p] = 0, \tag{3a}$$
$$\mathrm{E}[a_p a_q] = 0, \tag{3b}$$
$$\mathrm{E}[a_p a_q^*] = F(\omega_p)\delta_{pq}, \tag{3c}$$

where $\mathrm{E}[\cdot]$ denotes expectation, superscript * denotes complex conjugate, F represents the spectral power density of the diffuse field (Lobkis & Weaver, 2001), and δ is the Kronecker delta function. Since a_n exists independently of direction, equations (3a)-(3c) satisfies all three components of a fully diffuse wavefield. Therefore, using a single component wavefield (equation (2)) form is representative, which is also a commonly used way by previous researchers (Lobkis & Weaver, 2001; Weaver & Lobkis, 2004). However, assessing the waveform diffuseness using the time domain equations (3a)-(3c) is impractical due to the unavailability of the precise subsurface structure required for computing eigenfunctions, especially at high frequencies. We therefore derive in section (2.2) three equivalent expressions in the frequency domain that can be used to evaluate the modal amplitudes, circumventing the requirement for the eigenfunctions.

2.2 Characteristics of diffuse wavefield in the frequency domain

Following X. Liu and Ben-Zion (2016), a truncated diffuse waveform in the frequency domain can be expressed as

$$\phi(\mathbf{r}, \omega) = \mathscr{F}\{\psi(\mathbf{r}, t)\mathrm{rect}[t/T]\} = \sum_n a_n u^{(n)}(\mathbf{r}) T \mathrm{sinc}\left[\frac{(\omega - \omega_n)T}{2}\right], \tag{4}$$

where T is window length, $\mathscr{F}\{\cdot\}$ represents Fourier transform and $\mathrm{rect}[\cdot]$ is the boxcar function. Here, the diffuse waveform $\psi(\mathbf{r}, t)$ can be any component. For sufficiently long T, the sinc function can be effectively approximated by a Kronecker delta. In this case, for any frequency $\omega = \omega_p$, the truncated recording is simplified as

$$\phi(\mathbf{r}, \omega_p) = a_p u^{(p)}(\mathbf{r}) T. \tag{5}$$

The expectation of a seismic record in the frequency domain can be estimated by using numerous non-overlapping waveform segments,

$$\mathrm{E}[\phi(\mathbf{r}, \omega_p)] = \mathrm{E}[a_p] u^{(p)}(\mathbf{r}) T. \tag{6}$$

By adopting $\mathrm{E}[a_p] = 0$ to the above equation, we obtain $\mathrm{E}[\phi(\mathbf{r}, \omega_p)] = 0$, which means we are able to access criterion (3a) by computing the expectation of waveform spectra. Furthermore, considering that normal mode eigenfunctions $u^{(p)}(\mathbf{r})$ are not always zero, the observation of $\mathrm{E}[\phi(\mathbf{r}, \omega_p)] = 0$ across all frequencies implies $\mathrm{E}[a_p] = 0$. Therefore, $\mathrm{E}[a_p] = 0$ is equivalent to $\mathrm{E}[\phi(\mathbf{r}, \omega_p)] = 0$. For a more convenient evaluation, we construct a dimensionless quantity $A(\mathbf{r}, \omega_p)$ by normalizing the L2-norm of $\mathrm{E}[\phi(\mathbf{r}, \omega_p)]$. The expression is given by

$$A(\mathbf{r}, \omega_p) = \frac{|\mathrm{E}[\phi(\mathbf{r}, \omega_p)]|^2}{\mathrm{E}[|\phi(\mathbf{r}, \omega_p)|^2]} = 0. \tag{7}$$

Applying similar operations to the covariance of $\phi(\mathbf{r}, \omega_p)$ and $\phi(\mathbf{r}, \omega_q)$, we obtain

$$\mathrm{E}[\phi(\mathbf{r}, \omega_p)\phi(\mathbf{r}, \omega_q)] = \mathrm{E}[a_p a_q] u^{(p)}(\mathbf{r}) u^{(q)}(\mathbf{r}) T^2. \tag{8}$$

Therefore, $\mathrm{E}[a_p a_q] = 0$ is equivalent to $\mathrm{E}[\phi(\mathbf{r}, \omega_p)\phi(\mathbf{r}, \omega_q)] = 0$. A dimensionless form $B(\mathbf{r}, \omega_p, \omega_q)$ corresponding to equation (3b) is

$$B(\mathbf{r}, \omega_p, \omega_q) = \frac{|\mathrm{E}[\phi(\mathbf{r}, \omega_p)\phi(\mathbf{r}, \omega_q)]|^2}{\mathrm{E}[|\phi(\mathbf{r}, \omega_p)|^2]\mathrm{E}[|\phi(\mathbf{r}, \omega_q)|^2]} = 0. \tag{9}$$

In addition, the covariance of $\phi(\mathbf{r}, \omega_p)$ and $\phi^*(\mathbf{r}, \omega_q)$ is

$$\mathrm{E}[\phi(\mathbf{r}, \omega_p)\phi^*(\mathbf{r}, \omega_q)] = \mathrm{E}[a_p a_q^*] u^{(p)}(\mathbf{r}) u^{(q)*}(\mathbf{r}) T^2. \tag{10}$$

If $p \neq q$, $\mathrm{E}[a_p a_q^*] = 0$ is equivalent to $\mathrm{E}[\phi(\mathbf{r}, \omega_p)\phi^*(\mathbf{r}, \omega_q)] = 0$. If $p = q$, $\mathrm{E}[a_p a_q^*] = F(\omega_p)$ is equivalent to $\mathrm{E}[\phi(\mathbf{r}, \omega_p)\phi^*(\mathbf{r}, \omega_q)] = F(\omega_p)[u^{(p)}(\mathbf{r})T]^2$. A dimensionless form $C(\mathbf{r}, \omega_p, \omega_q)$ corresponding to equation (3c) is

$$C(\mathbf{r}, \omega_p, \omega_q) = \frac{|\mathrm{E}[\phi(\mathbf{r}, \omega_p)\phi^*(\mathbf{r}, \omega_q)]|^2}{\mathrm{E}[|\phi(\mathbf{r}, \omega_p)|^2]\mathrm{E}[|\phi^*(\mathbf{r}, \omega_q)|^2]} = \delta_{pq}. \tag{11}$$

To sum up, equations (3a)-(3c) are equivalent to equations (7), (9), and (11). By retrieving all possible ω_p and ω_q for these equivalent expressions, we can obtain a dimensionless vector $\mathbf{A}$, along with dimensionless symmetric matrices $\mathbf{B}$ and $\mathbf{C}$. If and only if a waveform $\psi(\mathbf{r}, t)$ is fully diffuse, $\mathbf{A}$ is a zero vector, $\mathbf{B}$ is a zero matrix, and $\mathbf{C}$ is an identity matrix. In contrast, if any of these three conditions are not met, the evaluated waveform is not fully diffuse. In this case, elements in $\mathbf{A}$, $\mathbf{B}$, and $\mathbf{C}$ span the range from 0 to 1 according to the Jensen's inequality and the Cauchy–Schwarz inequality,

$$0 \leq A(\mathbf{r}, \omega_p) \leq 1, \tag{12a}$$

$$0 \leq B(\mathbf{r}, \omega_p, \omega_q) \leq 1, \tag{12b}$$

$$0 \leq C(\mathbf{r}, \omega_p, \omega_q) \leq 1. \tag{12c}$$

Additional details of the above equations are provided in the supporting information (Text S1 and S2).

2.3 Multitaper spectrum analysis

In practical applications, the window length T can be insufficient, leading to an inadequate approximation of the Kronecker delta by a sinc function. This limitation introduces inaccurate estimation of the spectrum ($\phi(\mathbf{r}, \omega)$) of the target signal due to spectrum leakage caused by the side lobes of the sinc function. The leakage can affect the assessment of criteria $\mathbf{A}$, $\mathbf{B}$, and $\mathbf{C}$. To mitigate this effect, we employ the multitaper spectrum analysis technique proposed by Thomson (1982). In comparison to spectral estimates obtained using the rectangular window function as shown in equation (4), the multitaper spectrum analysis utilizes multiple orthogonal tapers. The spectrum is subsequently constructed by taking a weighted sum of these single-tapered periodograms. The multitaper technique has proven effective in reducing spectral leakage and is used commonly in various disciplines including geophysics (e.g., Park et al., 1987; Simons et al., 2000; Prieto et al., 2007; Babadi & Brown, 2014). In this study, we adopt the multitaper spectrum analysis technique of Riedel and Sidorenko (1995), which uses sinusoidal tapers. Compared with the widely used Slepian tapers, sinusoidal tapers provide better flexibility and adaptability to data by allowing selecting the number of tapers without any limitation on the frequency bandwidth of the signal (A. Kuvshinov & Olsen, 2006; A. V. Kuvshinov, 2008; Tian et al., 2022).

2.4 Proxies for quantitative evaluation of diffuseness

To obtain $\mathbf{A}$, $\mathbf{B}$, and $\mathbf{C}$ of observed waveform recorded by a seismograph, we first divide the time series into N non-overlapping segments, where N should be sufficiently large (e.g., $N \geq 30$) to enable reliable statistical analysis. We then compute the multi-tapered spectra of the N waveform segments and construct $\mathbf{A}$, $\mathbf{B}$, and $\mathbf{C}$ using equations (7), (9), and (11). To assess their deviations from the desired zero vector, zero matrix, and identity matrix for a fully diffuse waveform, one can evaluate the condition numbers, correlation coefficients, and residuals of these matrices.

The first option is to compare the matrix condition numbers of the three observed conditions and their target objects. For example, for condition $\mathbf{C}$, we can compute the condition number of matrix $\mathbf{C}$ to assess its proximity to an identity matrix. However, this proxy is not applicable to vector $\mathbf{A}$. Moreover, an identity matrix needs to be added to condition $\mathbf{B}$, which aims for a zero matrix, before computing the condition number to avoid singularity. This approach also depends on the size of the matrix, which can vary considerably depending on the duration and sampling rate of the data.

The second choice is to calculate the correlation coefficients, such as Pearson correlation coefficient or RV coefficient (Smilde et al., 2009; Robert & Escoufier, 1976), between the three observed conditions and their target objects. These coefficients are commonly used to quantify the proximity between two sets of data. However, the correlation coefficient is singular for zero vectors or matrices, rendering it unsuitable for calculating the proxies of conditions $\mathbf{A}$ and $\mathbf{B}$.

The last alternative is to compute the residuals of the three observed conditions and their target objects. This method is intuitive, efficient, and widely applied in various disciplines. By quantifying the norm of residuals, such as the most commonly used L2-norm, one can measure the deviation from observed and the target value. However, the conventional L2-norm calculation may lack sensitivity to certain key pattern differences in the residual matrix, potentially leading to biased evaluations.

Good proxies for evaluating waveform diffuseness should exhibit the characteristics of simplicity, sensitivity to key pattern differences, applicability to both vectors and matrices, and independence from matrix dimensions. Therefore, quantifying the residuals is considered the most promising approach. To overcome the disadvantages mentioned above, we propose an improved Root Mean Square (RMS) function that quantifies the results generally between 0 and 1, making them independent of the size of conditions $\mathbf{A}$, $\mathbf{B}$, and $\mathbf{C}$. The proxy calculated by the improved RMS function is

$$P = \sqrt{\frac{\sum_{j=1}^{N}(w_j x_j)^2}{N}}, \tag{13}$$

where $x_j = |A_j^{\mathrm{obs}} - A_j^{\mathrm{tar}}|$ is the jth element of the absolute value of the residual of the observed and target of condition $\mathbf{A}$ with size of $1 \times N$, w_j is the weight of x_j. This is defined as

$$w_j = \Big(\frac{1}{2s+1}\sum_{k=j-s}^{j+s} x_k\Big)/\mathrm{mean}[\mathbf{x}], \tag{14}$$

where s is the scale of the window $(2s+1)$ of the weight. Since condition $\mathbf{A}$ is dimensionless, $0 <= x_j <= 1$ for all $\mathbf{x}$. In addition, all w_j are distributed around 1, therefore $0 <= P <= 1$ for most waveform data. Smaller values of P indicate the recorded waveform better satisfies the characteristics of a diffuse field. By defining a dimensionless scale factor $s_{\mathrm{f}} = s/N$, we have $0 <= s_{\mathrm{f}} <= 1$. Varying the scale factor assigns different weights, leading to variations in the calculated values. Equation (13) thus defines a scale-dependent RMS function (sRMS) applicable to both vectors and matrices. For matrix data, the computation can be extended by incorporating equations (13) and (14) into equations S18 and S19 (see Text S3). Introducing a smaller scale factor places greater emphasis on the deviation of each element from the collective characteristics of all elements. Conversely, a larger scale factor brings the weighted element closer to its original value. In particular, when $s_{\mathrm{f}} = 1$, sRMS is equivalent to the traditional RMS.

To determine the optimal choice of $s_{\rm f}$, we analyze continuous waveform data recorded by node R3010 at the SGB site (Figure 1) over a span of two days. The waveform is divided into 2880 non-overlapping 60-second segments. Figure S1a illustrates the variation of proxy values for conditions **A**, **B**, and **C** with respect to $s_{\rm f}$. The results exhibit a general downward trend, with the proxy values decreasing and asymptotically approaching horizontal lines as $s_{\rm f}$ increases. Examining the first-order derivative curves (Figure S1b), we observe that both small and large values of $s_{\rm f}$ involve a trade-off between stability and sensitivity. We consider the corner point of the first-order derivative curve as the optimal choice of $s_{\rm f}$ (Figure S1c), which balance the stability and sensitivity of the proxy. The distributions of the three proxies of the 2880 waveform segments show good consistency, further reinforcing the reliability of the chosen $s_{\rm f}$ (Figure S1d).

3 Results

In this section, we provide a comprehensive evaluation of the effectiveness of our proposed method using both synthetic and real seismic data. We begin by demonstrating that the method can accurately quantify the diffuseness of synthetic diffuse noise, as well as the consistency in the evaluation of three-component measured seismic records. Subsequently, we present examples of non-diffuse signals by applying the method to recorded ground motions generated by a local earthquake, a car traffic event, and a wind gust. Finally, we extend the analysis of waveform anatomy conducted by Meng et al. (2019) to evaluate whether the detected Random Noise (RN) exhibits the characteristics of a diffuse field.

3.1 Synthetic diffuse noise

To demonstrate the application of our methodology using seismic records, we first generate synthetic random noise that is also diffuse. This is done first by performing Fourier transform of a low amplitude 500 s vertical component waveform that was recorded at night on node R3010 (its location reference Figure 1b). We then replace the phase term with a uniform distribution of values ranging from 0 to 2π. Finally, an inverse transformation is performed on the resulting amplitude spectrum (Figure 2a) and randomized phase thus obtaining the synthetic diffuse noise (Figure 2b) used for test. These operations ensure that the synthetic waveform would be stationary and random (Figure 2c), show no coherence across different frequencies, and therefore be diffuse.

To quantify the conditions **A**, **B** and **C**, we divide the waveforms into $T = 1$ s non-overlapping sub-windows (unless otherwise specified, the length of sub-window in this paper is 1 second) and stably estimate the spectrum of each window using the multitaper spectrum analysis technique (Riedel & Sidorenko, 1995). Choosing a sub-window length of 1 s allows us to analyze high-frequency signals above 1 Hz (in the case of zero frequency neglect), which ensures that when we stack at least 30 sub-windows, the total signal length will not be too long to include more event signals and contaminate the estimation of interest signals. Then, the spectra and the outer products with themselves and their conjugates are averaged according to equations (7), (9) and (11). Finally, the corresponding results are shown in Figures 2d-2f. Since the data is sampled at a rate of 500 Hz, we are guaranteed to resolve 250 frequencies in interval $[1, 250]$ Hz in the case of a sub-window length of 1 s. We find that all elements of conditions **A** and **B** and elements on the non-diagonal of condition **C** are nearly 0, while the diagonal elements of condition **C** are 1. We further compute their proxies using the sRMS with $s_{\rm f} = 0.05$ (Figures 2d-2f). As expected, the proxies P_A, P_B and P_C corresponding to conditions **A**, **B** and **C** are very small, all less than or equal to 0.005, indicating that the synthetic waveform in Figure 2b is sufficiently diffuse.

Persistent and intensive single-frequency interference are commonly observed in seismic records due to the electric noise and other problems. Such interference can severely

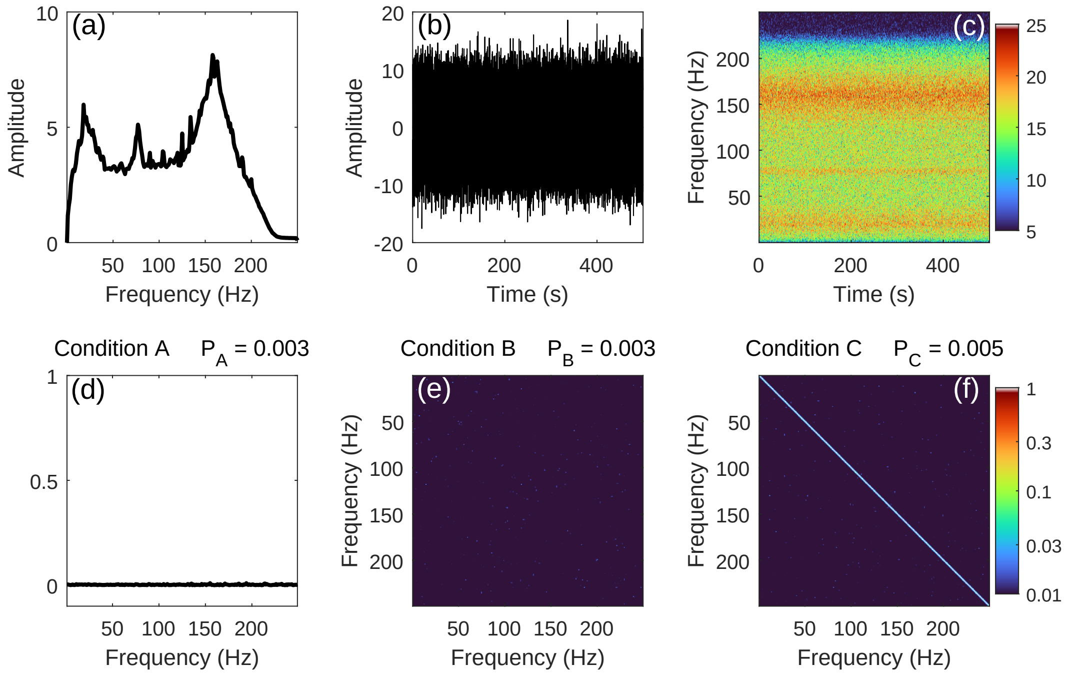

Figure 2. (a) The observed amplitude spectrum of a 500 s vertical component waveform recorded by node R3010 at night. (b) Synthetic diffuse noise generated using the spectral amplitude in (a) with randomized phase. (c) The spectrogram of the synthetic diffuse noise. (d-f) The conditions **A**, **B** and **C** of the synthetic diffuse noise in (b).

impede efforts to retrieve subsurface structures from the diffuse field. To test whether the proposed method can quantify such signals, we add 50 Hz and 120 Hz single-frequency interference to the diffuse noise waveform shown in Figure 2b. The results are presented in supporting information Figure S2. In Figure S3, we further show the results obtained by doubling the interference intensity. Although the interferences from the added single-frequency sources are not easily identifiable in the waveforms (Figure S2b and Figure S3b), the pulses at 50 Hz and 120 Hz of the condition **A** (Figures S2d and S3d) clearly reduce the diffuse characteristics of the original diffuse noise in Figure 2b. Specifically, the evaluation proxies of conditions **A**, **B**, and **C** shown in Figure 2, Figures S2, and S3 are proportional to the amplitude of the interference intensity. This illustrates that our method not only correctly identifies data containing such interference patterns as diffuse or non-diffuse, but also provides a quantitative measurement of the magnitude of their effect on the diffuse wave.

3.2 Evaluating three-component ambient noises

To further validate our method using three-component seismic waveforms, we analyze the seismic waveforms recorded by node 156 in the 9A network on December 14, 2017, 00:02:20-00:05:00 (UTC time), which is collocated with the dense vertical array shown in Figure 1b. The waveforms include pre-seismic ambient noises and a local M 2.1 earthquake with its coda waves (Figure S4). Figure 3 presents the 1-minute pre-seismic noise of two horizontal components (GP1 and GP2) and the vertical component (GPZ). We evaluate the three components separately and observe consistent characteristics indicative of a diffuse wavefield. Specifically, condition **A**, **B**, **C** approximate a zero vector, a zero matrix, and an identity matrix, respectively. The proxies P_A, P_B, and P_C

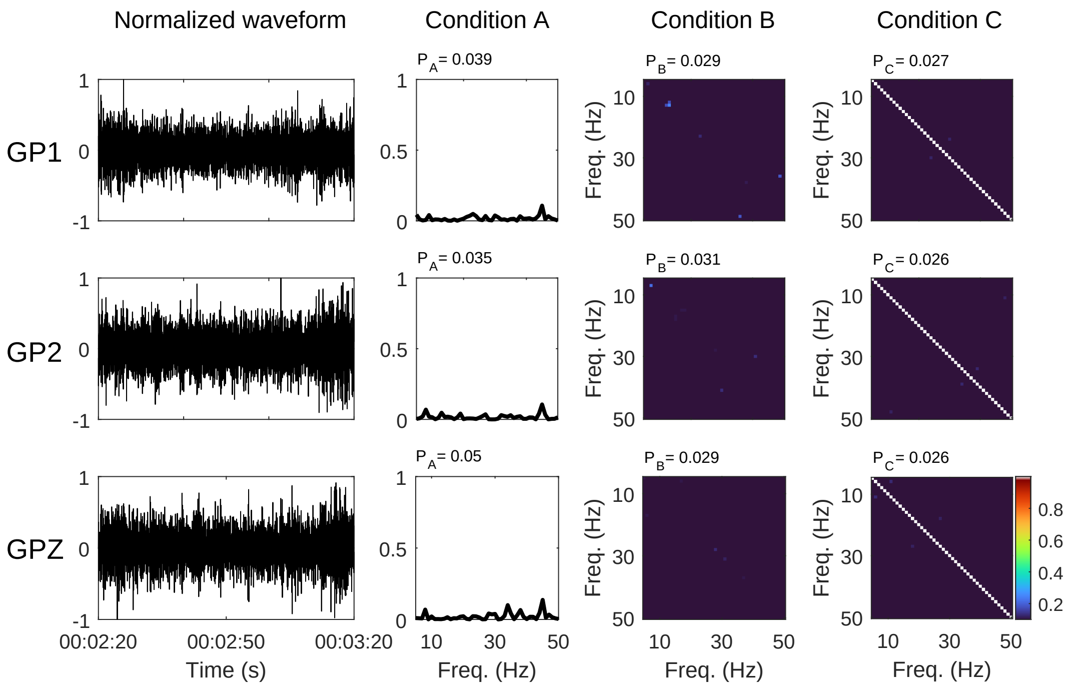

Figure 3. Evaluation results for ambient noise segments of the three-component waveforms recorded by station 156 on December 14, 2017, 00:02:20-00:03:20 (UTC time) in the frequency range of 5-50 Hz. The first and second rows correspond to results for the horizontal components GP1 and GP2, respectively, while the third row correspond to the vertical component GPZ.

of the three components all exhibit small values. This consistency confirms the validity of our method in assessing the diffuseness of each seismic wave component.

The same analysis is performed on the coda waveform segments of the M 2.1 earthquake, which also exhibit characteristics of a diffuse wavefield in all three components. Details can be found in Figure S5, illustrating that the late three component coda waveform segments overall fit with diffuse wavefield characteristics are satisfactory, as indicated by small values for the P_A, P_B, and P_C proxies. Conversely, when one component does not satisfy the characteristics of the diffuse wavefield, the other two components are not diffuse as well. As shown in Figure S6, the evaluation results of the three components of the 40-second-long waveform segments dominated by ballistic waves show that strong correlations within the 5-30 Hz range, indicating that they do not meet the characteristics of a diffuse wavefield. While conditions **A**, **B** and **C** may display slight variations in characteristics across the three components in actual seismic record due to different sensor noise and coupling effects, it is noteworthy that all components consistently exhibit either large or small proxy values, which are able to distinguish between diffuse or non-diffuse waves. In practical applications, our method offers flexibility, allowing users to apply it either to single- or three-component data.

3.3 Evaluating non-diffuse waveforms

During the deployment at the SGB site, the dense seismic array recorded ground motions inducted by small local earthquakes, cars, airplanes, wind gusts, etc. To evaluate the performace of our method on non-diffuse waveform examples, we analyze the vertical waveforms of a few such sources recorded by node R3010 (Figure 1).

Figures 4a(I-V) show from the top to bottom the recorded waveform, the corresponding spectrogram, and the evaluated conditions **A**, **B**, and **C**, respectively. Notably in Figure 4a(III), we observe that condition **A** is not a zero vector. In Figures 4a(IV-V), the orangish square at the top left indicates coherent energy in the frequency range of 1-125 Hz, which is associated with the earthquake signal that consistently appear in many sub-windows in the evaluation. Additionally, the greenish square at the bottom right indicates coherent energy in the frequency range of 125-200 Hz. This coherent energy is attributed to a wind gust event that occurred between 25 and 40 seconds, which coincided with the recording of the earthquake signals in Figures 4a(I-II). Consequently, both evaluation proxies for conditions **B** and **C** yield values of approximately 0.5, providing evidence that the earthquake waveform exhibits non-diffuse characteristics.

The same analysis is conducted on the ground motions induced by car traffic and wind gust, and the results are presented in Figures 4b(I-V) and 4c(I-V) respectively. In Figure 4b(III), although the evaluation proxy for condition **A** is relatively small, the large proxies for conditions **B** and **C** suggest that the car-induced vibration record is non-diffuse. Moving on to Figure 4c(I-V), both the visual observations and the calculated indexes for conditions **A**, **B**, and **C** indicate that the wind-induced vibration record does not exhibit the characteristics of a diffuse field.

The non-diffuse characteristics of the above three ground motions can be attributed to the fact that the ballistic waves caused by the events dominate the signal window. If we move the window of interest back, for example by examining the late event signals of a car, we can find that its coda waves can also exhibit diffuse characteristics when the conditions are met, as shown in the Figure S8. Similar analysis can be applied to the coda of small earthquake events, which will be introduced later in subsection 4.3.

3.4 Evaluation of anatomical results of continuous seismic waveforms

Meng et al. (2019) developed a methodology to detect different types of wave packages in continuous seismic records including Random Noise (RN). In this subsection we evaluate whether the detected RN exhibits the characteristics of a diffuse field. The waveform analysis method includes analyses of the cross-correlation of waveform segments and amplitude spectra comparisons. The hourly RN is quasi-stationary, and the results cluster tightly in the parameter space of cross-correlation coefficients and L2 norm deviations from the mean spectra of RN candidates (Meng et al., 2019). To estimate the extent to which wavefields in different time windows are diffuse, we build on the waveform analysis method and analyze the data recorded by the dense deployment.

Figure 5 presents the raw waveforms (a), spectrograms (b) and corresponding detected RN (c) of example hours recorded by node R3010 on May 26, 2014 from 14:00 to 15:00 (local time). On the raw waveforms, we perform a classification analysis using the method developed by Meng et al. (2019). We then use a sliding window of length 30 s with an overlap of 29 s to analyze the diffuse field characteristics of the RN. The evaluation proxies of conditions **A**, **B** and **C** corresponding to each sliding window are shown at the center of the window with red, orange and blue dots in the lower panel of Figure 5c. The bottom right panels of Figure 5c show the mean and standard deviation of the evaluation metrics. These results demonstrate that the RN signals separated by Meng et al. (2019) exhibit the characteristics of a diffuse field. The small standard deviations of the evaluation proxies of the RN signals indicate their temporal stability and robustness. Applying the same analysis to non-random noise and mixed signals from the raw waveform separated by Meng et al. (2019), the results (shown in Figures S7c, d) indicate that these two signal types do not exhibit the characteristics of a diffuse field.

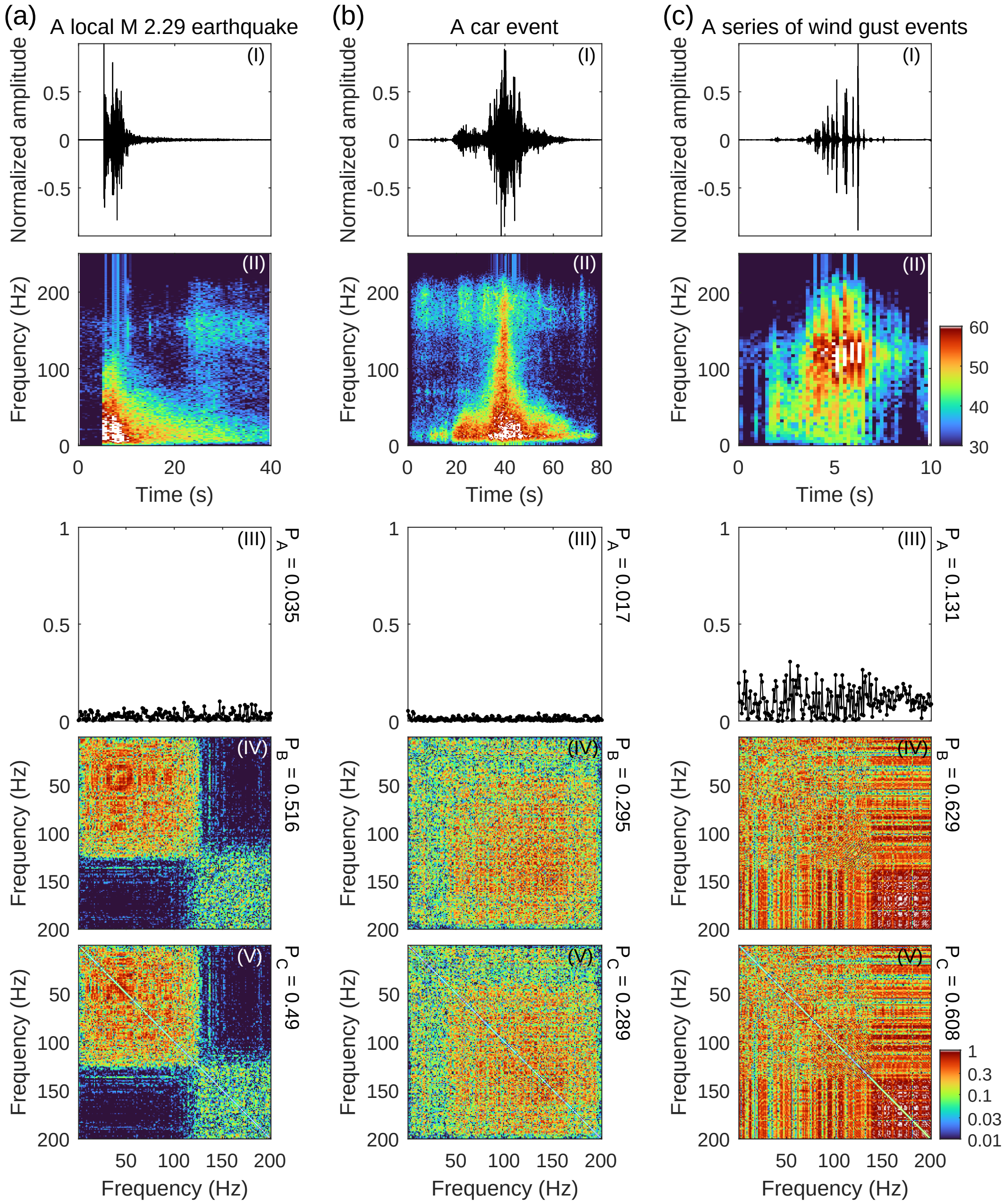

Figure 4. Examples of non-diffused waveforms recorded by node R3010. (a) The left column: The example of a local M 2.29 earthquake waveform. (b) The middle column: The example of a car event waveform. (c) The right column: The example of a series of wind gust event waveforms. From top to bottom, i.e., (I) to (V), each row represents the waveform, spectrogram, and conditions **A**, **B** and **C**, respectively.

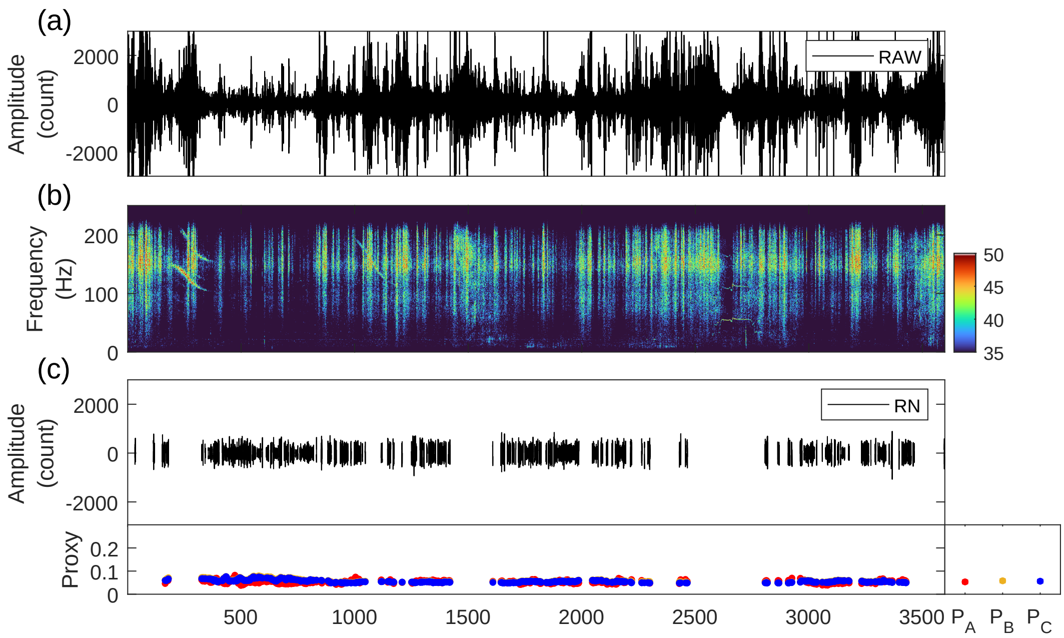

Figure 5. Examination of anatomical results of continuous seismic waveforms proposed by Meng et al. (2019). (a) The raw continuous seismic waveforms recorded by node R3010 on Julian day 146, 2014 from 14:00 to 15:00 (local time). (b) Corresponding spectrogram of the waveform in (a). The upper panel of (c) shows the RN signals separated from waveform in (a). The degree of diffuseness of these signals are evaluated in a sliding window of length 30 s with an overlap of 29 s, and the results are presented in the lower panels of (c). The red, orange and blue points are the evaluation proxies corresponding to the conditions **A**, **B** and **C**, respectively. The bottom right panel of (c) shows the mean of the evaluation proxies with standard deviations.

4 Discussion

We present the EDWav method for evaluating the diffuseness of wavefields by quantifying the stationarity and cross-frequency coherence of the waveform. The method can be easily implemented in the frequency domain by using equations (7), (9), and (11). We have demonstrated the validity and effectiveness of this method through tests on synthetic diffuse noise, three non-diffuse waveforms, and RN obtained from previous analysis on waveform anatomy. Below we provide additional details on the EDWav method and discuss insights it provides in seismic imaging studies.

4.1 Comparison of sRMS and RMS approaches

In subsection 2.4, we introduce the scale-dependent Root-Mean-Square (sRMS) approach to evaluate the magnitude of residuals between observed and target condition. The sRMS method builds upon the root-mean-square (RMS) function but adds an adjustable scaling factor. According to equations (13) and (14), a smaller scale factor causes the sRMS to reflect the deviation of each element from the overall characteristics of all elements. Conversely, a larger-scale factor weights each element closer to its original value. This relationship is illustrated and confirmed by the curve variations in Figure S1a. Compared to the conventional RMS approach, the sRMS method is advanced in flexibility and sensitivity, and it is better suited to evaluate the magnitude of residuals.

To demonstrate the utility of the sRMS approach, we conduct comparative experiments using two waveforms recorded by the same station at different times, as depicted in Figures 6a and d. The waveform shown in Figure 6d displays a higher occurrence of tremor-like wiggles, indicating a less diffuse nature compared to Figure 6a. This is confirmed by their condition **B** shown in Figures 6b and e. Figure 6b reveals that discrete bright spots are evenly distributed across the image. These spots exhibit consistent brightness (value) and appear relatively dark (small), which indicates that the waveform in Figure 6a aligns with characteristics of a diffuse wavefield. However, Figure 6e reveals a distinct pattern where three continuous bright rays concentrate from the upper-left corner to the lower-right corner. This concentration of bright rays suggests that the waveform in Figure 6d is significantly influenced by non-stationary sources, potentially associated with air traffic disturbances (Meng & Ben-Zion, 2018). Subsequently, we apply the RMS approach (i.e., sRMS with $s_{\mathrm{f}} = 1$) to calculate the proxy of their condition **B**. Interestingly, we find that RMS yield similar results for both waveforms, with values of 0.042 and 0.043, respectively. Such similarity in the results can be attributed to the inherent insensitivity of RMS, as it does not consider the distribution position of the data (i.e., the bright spots and rays in Figure 6b and e). Consequently, relying on the RMS function to distinguish between diffuse and non-diffuse waveforms poses a risk.

Using the sRMS function can mitigate the insensitive shortcoming of the RMS function. As shown in the bottom-left corner of Figures 6c and f, the proxies of condition **B** for the two waveforms display considerable difference, which are 0.043 and 0.093, respectively. The key reason behind the advantage of sRMS lies in its ability to assign weights to the residuals for analysis. This is accomplished by comparing the ratio of the mean value of the data within a specific range surrounding the residuals under investigation to the mean value of the overall residuals, as indicated by equation 14. By applying sRMS weighting to Figures 6b and e, the resulting images depicted in Figures 6c and f highlight a notable enhancement in the representation of continuous and trended bright spots, while displaying reduced sensitivity to discrete bright spots. Since non-diffuse waveforms often have correlated frequency components that appear in pairs or groups (as shown in Figures 4 and 6b), these characteristics of sRMS can well distinguish between diffuse and non-diffuse waveforms. Therefore, sRMS proves to be a suitable method for calculating the proxy in the EDWav method.

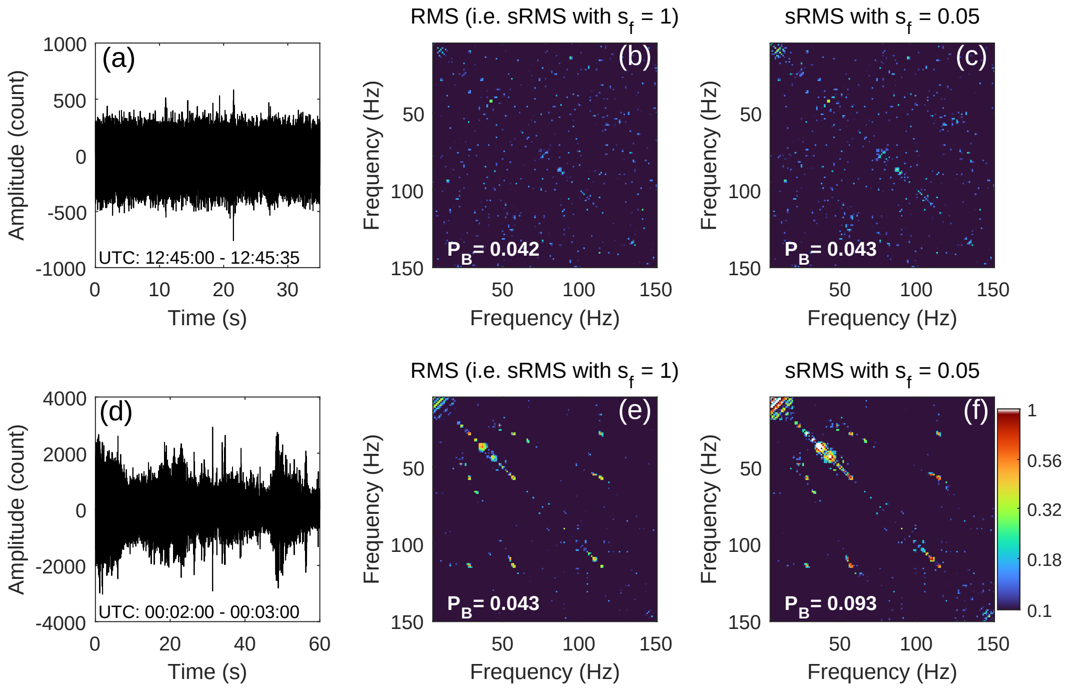

Figure 6. Comparison of sRMS and RMS in calculating evaluation proxy. (a) and (d) are the two waveforms recorded by node R3010 on Julian day 131, 2014. The difference visible to the naked eye is that (a) is more characteristic of the diffuse wavefield than (d). (b) and (e) are the conditions **B** of (a) and (d), respectively. (c) and (f) are the transformed image from (b) and (e) by the sRMS method, respectively.

4.2 Insights into preprocessing procedures of ambient noise imaging

The retrieval of Green's function in ambient noise studies requires a diffuse wavefield. However, the recorded ambient noise usually contains a lot of interference from non-diffuse signals, such as car traffic, trains, storms, wind turbines, and air traffic (Meng & Ben-Zion, 2018; Meng et al., 2019, 2021). To effectively suppress signals from tectonic, anthropogenic, and environmental sources, a crucial preprocessing step involves waveform normalization in both the time and frequency domains. This can be achieved through techniques such as one-bit filtering and whitening, respectively. The application of normalization has been widely used and proved to be successful Bensen et al. (2007) and many subsequent papers (e.g., Prieto et al., 2011; J. Wang et al., 2019; Xie et al., 2020). In this section, we quantitatively evaluate the waveform diffuseness of a local earthquake before and after the various normalization approaches proposed in Bensen et al. (2007). This analysis aims to clarify the effectiveness of different normalization techniques and the underlying reasons for their varying performance.

As shown in Figure 7, the leftmost panel in the first row (a) presents a non-diffused waveform with a duration of 100 s. This is a local M 2.0 earthquake that occurred on 15 May 2014, recorded by node R2509. The epicenter is shown in the red circle in Figure 1a. The seismic waveform is evaluated with the discussed techniques and the results are shown in the second to fourth columns of Figure 7a. From condition **A**, we can find that this section of the waveform is interfered by many strong single-frequency signals, as evidenced by spikes at 50 Hz, 75 Hz, 100 Hz, 125 Hz and 150 Hz. In addition, condition **B** and condition **C** exhibits clustered bright spots, which deviates from the expected characteristics of a zero matrix and an identity matrix, respectively. The large evaluation proxies P_A, P_B, and P_C further support the conclusion that the waveform lacks diffuseness.

We then apply one-bit, clipping, and running absolute mean algorithms to normalize the seismic waveform in the time domain. The processed waveform and corresponding evaluation results are shown in Figures 7b-d. Upon examination of Figure 7c, the bright images and large proxies of conditions **A**, **B**, and **C** reaffirm the assertion made by Bensen et al. (2007) that the clipping algorithm is unsuccessful in improving the cross-correlation results. This can be attributed to the presence of many step-function-like waveform segments that emerge when the peaks and valleys are flattened beyond the threshold during the clipping process. The sudden transitions, which can be approximated by step functions, generally follow a f^{-1} spectrum. They frequently occur in 16 to 36 seconds (Figure 7c) and therefore exacerbate cross-frequency coherence and non-diffuse characteristics in the frequency bands from 10 to 35 Hz. Similar to the one-bit filtering approach (Figure 7b), the running absolute mean normalization method (Figure 7d) can also significantly reduce the proxies of condition **B** and condition **C**. This indicates its ability to effectively suppress non-stationary and non-diffuse seismic signals.

However, none of the normalization algorithms in the time domain show significant improvements in condition **A**. The presence of spikes in this condition remains unresolved using these techniques (Figures 7b-d). To tackle this issue, normalization in the frequency domain, specifically employing the spectral whitening algorithm, proves effective in suppressing the spike amplitudes (Figure 7e). Nevertheless, solely performing the frequency domain normalization of the earthquake waveform still leads to strong non-diffuse characteristics in conditions **B** and **C**.

The aforementioned quantitative analyses provide valuable insights into the effects of the normalization techniques. Specifically, the time-domain normalization primarily targets the suppression of weights associated with strong and non-diffuse signals. The frequency-domain normalization flattens the spectral amplitude over the frequency range of interests and combats degradation caused by persistent homogeneous sources. We further follow the preprocessing procedures of several representative ANI studies (Bensen et al., 2007; Yang et al., 2007; J. Wang et al., 2019; Xie et al., 2020; X. Xia et al., 2021) by performing one-bit and then whitening algorithms to the earthquake waveform. Such procedures result in significantly improved conditions **A**, **B** and **C** (Figure 7f), as evidenced by the smallest proxies in each column of Figure 7.

In the field records, not all waveforms contain strong single-frequency interference signals. If the proxy of condition **A** is already small, then the spectral whitening operation is unnecessary in the preprocessing of ANI. Similarly, if earthquakes, instrumental irregularities, or other nonstationary wiggles are absent, the normalization operation in the time domain can also optionally be omitted when both proxy conditions **B** and **C** are adequately small. Waiving these processes by identifying the diffuse wave segments brings two advantages. On the one hand, it can simplify the processing steps, reduce the data redundancy, and improve the computational efficiency for ANI. More importantly, we are able to recover the reliable amplitude from waveform interferometry using the waveforms without disturbance of amplitude by the normalization. This is essential to extract attenuation parameters of the subsurface structures. We therefore propose integrating the EDWav as a perprocessing step of ANI to identify the diffuse wave segments with relative strong energy, such as the coda waves of earthquake or wavefield before and after traffic events (an example of a car event coda evaluation can be found in Figure S8, which supports the search for relative strong energy waveforms from signals in the late traffic events). This method offers the advantage of quantifying waveform diffuseness while also facilitating the retrieval of improved EGFs for imaging purposes. This type of idea of improving EGFs recovery by identifying and stacking favorable cross-correlations has also recently been applied to deciphering volcanic whispers (Makus et al., 2023) and extracting body wave phases from the depth Earth (Pedersen et al., 2023).

4.3 Application of EDWav in retrieving dispersion and attenuation

The coda of large earthquakes ($M \geq 7$) can last for a long duration, providing rich seismic data and can be used to extract the EGFs between stations through seismic interferometry (Campillo & Paul, 2003; Paul et al., 2005). However, large earthquakes are infrequent and predominantly occur along plate boundaries. Moreover, some studies have shown that their constituents are complex and lack diffuseness over long periods (Maeda et al., 2006; Poli et al., 2017; Sens-Schönfelder et al., 2015). Consequently, relying solely on these rare events and retrieving their diffuse components for seismic imaging is risky for mobile and temporary seismic arrays. Alternatively, small earthquakes occur much more frequently and are widely distributed, as indicated by Gutenberg-Richter statistics (Gutenberg & Richter, 1944), and typically occur shallower, with waveform energy more likely to be equipartitioned by scatterers. Therefore, in this section, we apply the EDWav method to the coda waves of a M 2.2 earthquake recorded by the spatially dense array (Figure 1b), and use the identified diffuse waves for retrieving the dispersion and attenuation of subsurface structures.

The small earthquake occurred in the southern end of the SJFZ on 11 May 2014. An example waveform recorded by node R2010 is shown in Figure 8a. To distinguish between the ballistic and coda waves, we employ the EDWav method on two adjacent sliding windows, each spanning 60 seconds, for the waveform recorded by node R2010. The separation is achieved by the differentiation of the diffuseness proxies of the two windows (details are shown in Figure S9), we selected the non-diffuse ballistic wave window and the diffuse coda wave window. In order to select suitable nodes for reconstructing EGFs, we apply the coda window to all nodes in the SGB dense array, and observe that the seismic coda waves inside the sedimentary basin exhibit greater energy intensity and higher overall diffuseness degree compared to those outside the basin (Figure S10). We therefore select the 142 nodes within the basin as a sub-array, represented by the red circles in Figure 1b, for the purpose of reconstructing EGFs using the cross-correlation functions. As depicted in Figure 8d, the mean values of P_A, P_B, and P_C of the ballistic and

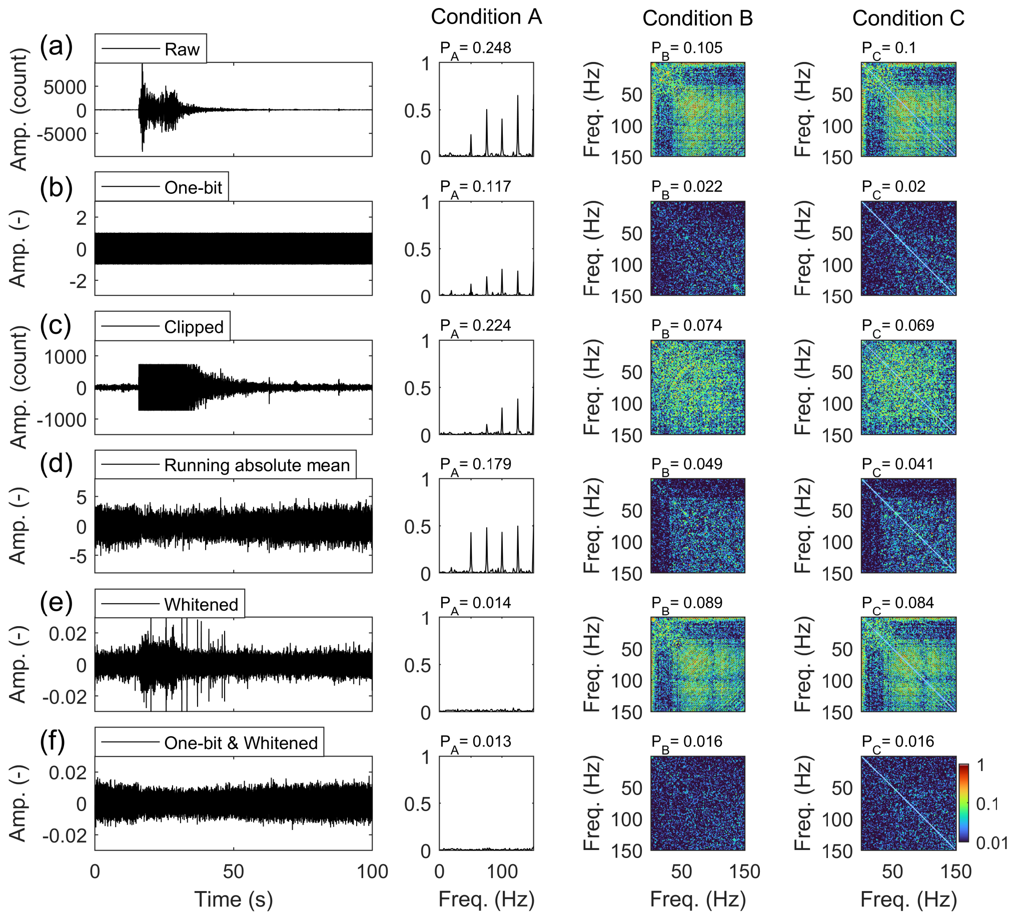

Figure 7. Inspection of time and frequency domain normalization methods for the local M 2.0 earthquake shown in Figure 1b. (a) The earthquake waveform recorded by node R2509 and its evaluation results of conditions **A**, **B** and **C**. (b-d) Waveforms and corresponding evaluation results after one-bit normalization, clipping, running absolute mean normalization and spectral whitening of the waveform in (a). (f) The waveform and corresponding evaluation results after one-bit normalization and spectral whitening of the waveform in (a).

coda waves of these 142 nodes exhibit clear separation with a value of 0.0625 and form two distinct clusters, indicating the correctness of our identification of diffuse coda waves and nodes selection.

Subsequently, we retrieve the EGFs using the 60-second-long ballistic and diffuse coda waves. For the ballistic wave of the earthquake (the blue waveform in Figure 8a), we follow Bensen et al. (2007) and adopt one-bit filtering and spectral whitening to suppress the non-diffuse components. The processing approach employed, as depicted in Figure 8b, does not produce clear surface wave signals in either the positive or negative lag time of the cross-correlation functions. Instead, prominent pulse signals are observed around zero time. This is due to the short waveform length, insufficient ambient noise, and the high incidence of seismic body waves propagating vertically along the fault below the array. In contrast, for the identified coda waves (the red waveform in Figure 8a), we directly compute the cross-correlation functions without employing any additional preprocessing procedures. The Rayleigh wave signals and the corresponding propagation effects have been well reconstructed (Figure 8e). The results show basically consistency with previous studies (Roux et al., 2016; Hillers et al., 2016) and the reference shown in Figure 8h, where cross-correlation functions were computed using continuous waveforms for the entire day and subjected to one-bit filtering and spectral whitening. It should be noted that the coda wave segments used are considered sufficiently diffuse (they have small diffuseness proxies, as shown in Figure 8d. In this context, 'sufficiently diffuse' indicates that the nonstationary component in the signals has a limited impact on the reconstruction of Empirical Green's Functions (EGFs) from cross-correlation functions, rather than being fully diffuse. Furthermore, the duration of the data compared to the reference for one day is considerably shorter, at only 60 seconds, enhancing the efficiency of extracting reliable EGFs from short seismic records.

To extract the dispersion curves, we utilize the recently developed Frequency-Bessel transform method (J. Wang et al., 2019; Li et al., 2021) on the three groups of aforementioned cross-correlation functions (Figures 8b, e, and h). As expected, the ballistic wave, characterized by its non-diffuse nature, does not yield a clear dispersion curve. However, for coda waves, we observe a clear and continuous dispersion curve for the Rayleigh wave within the frequency range of $7-15$ Hz, as illustrated in Figure 8f. The results again demonstrate good consistency with the reference dispersion (Figure 8i) obtained using continuous waveforms throughout the day. We note that while the dispersion curve derived from diffuse coda is adequately good for ANI, it may not necessarily outperform the dispersion curve computed from longer records using normalization as both methods effectively recover the phase information. We also conduct a test by randomly selecting a 60-second-long window of ambient noise. However, the attempt to obtain clear dispersion curve is unsuccessful (Figure S11). This is mainly due to the low energy of ambient noise, which requires much longer records to reconstruct EGFs. Nevertheless, our findings suggest that by identifying diffuse waves with strong energy, we can achieve comparable quality results using only minute-long records instead of data collected over an entire day. This indicates that these short records contain essential information for ANI, despite covering only a small portion of the continuous records. Consequentially, our results offer a possibility of advancing the workflow of ANI by integrating the ED-Wav method to identify the sparsely distributed high energy and diffuse waveform segments. By leveraging this approach, we can improve computing efficiency by avoiding the need to calculate cross-correlations of day-long records. Furthermore, it is possible to monitor the temporal change in the subsurface structures with high temporal resolution if there are frequent detections of qualified waveform segments, such as the coda waves of the foreshocks and aftershocks in a large earthquake sequence.

Since we do not introduce any normalization preprocessing for the coda waves prior to computing the cross-correlation functions, the reconstructed EGFs preserve reliable phase and amplitude at the same time. We therefore are able to extract not only the dis-

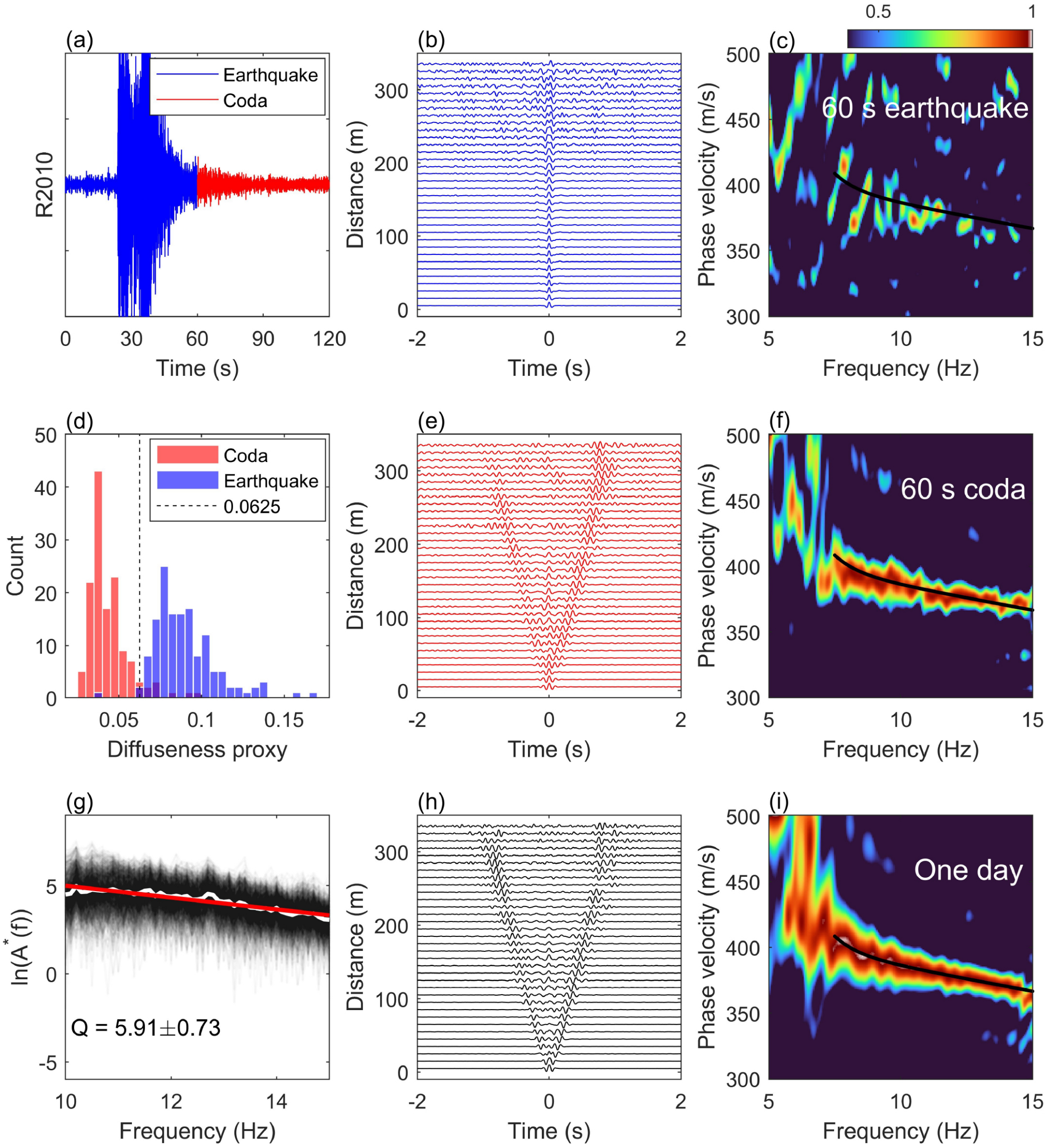

Figure 8. Coda cross-correlation and dispersion spectrum of a M 2.2 earthquake displayed in Figure 1b. (a) Example waveform of the earthquake recorded by node R2010. Blue and red represent the identified earthquake ballistic wave and coda wave, respectively. (d) The statistical histogram of diffuseness proxies of the ballistic and coda waves recorded by the 142 stations in the basin. The diffuseness proxy here refers to the mean value of P_A, P_B and P_C. The cross-correlation functions of ballistic waves, coda waves, and continuous records for one day are shown in (b), (e) and (h). For ease of display, we bin and average the cross-correlation functions for a distance increment of 10 m. The corresponding dispersion spectra are presented in (c), (f), and (i). (g) Amplitude spectra of the coda cross-correlation functions after geometric correction (black lines). The Thick white line shows the mean spectrum and the red line denotes the optimal model prediction with a Q-value of 5.91.

persion but also the attenuation of the subsurface structure from the EGFs in Figure 8e. Considering the geometrical spreading and attenuation effects, the recorded amplitude A of Rayleigh waves at distance r and frequency f is given by (Meng et al., 2021; Inbal et al., 2018)

$$A(r,f) = \frac{A_0}{\sqrt{r}} e^{-\frac{\pi f r}{cQ}}, \tag{15}$$

taking the natural logarithm of equation (15) gives

$$\ln A^*(f) = \ln A_0 - \frac{\pi r}{cQ} f, \tag{16}$$

where $A^*(f) = A(r,f)\sqrt{r}$, A_0 is the initial amplitude spectrum, c is the phase velocity, Q is the quality factor of Rayleigh wave. Under the assumption of frequency-independent Q-value, equation (16) illustrates the linear relationship between the logarithm of the corrected amplitude and the frequency. With the known r and derived c, the average Q-value of the study area and frequency band of interests can be obtained by perform a linear fitting analysis on the corrected cross-correlation amplitude spectra. To obtain reliable results, we select cross-correlation functions with a distance greater than 200 m to minimize the interference caused by body waves. Additionally, we only resolve Q-values higher than 10 Hz to avoid the amplitude distortion by the nodes with a lower sensitivity below 10 Hz. As shown in Figure 8g, the average Q-value of the basin is 5.91 ± 0.73, which is consistent with the results measured using vehicle signals in this area (Meng et al., 2021), indicating strong attenuation of the shallow subsurface sediments.

To further validate the dispersion and attenuation parameters extracted using the detected diffuse coda wave as described above, we compare our results with those obtained using a classical method (Prieto et al., 2009; Magrini & Boschi, 2021). This method derives subsurface dispersion and attenuation by minimizing the residual of the zero-order Bessel function with attenuation and the real part of coherency of the observed data, i.e.,

$$\varepsilon(f) = ||\mathrm{Re}[\gamma(f,r)] - J_0(\frac{2\pi f}{c} r) e^{-\alpha r}||^2, \tag{17}$$

where $\gamma(f,r)$ is the average coherency for station separation r, J_0 is the zero-order Bessel function for frequency f at distance r, $\alpha = \frac{\pi f}{cQ}$ is the frequency-dependent attenuation coefficient. To ensure consistency in comparison, we focus on the frequency band of $7-15$ Hz. Figures 9a and b persent the real part of the observed and predicted coherency, respectively, obtained through a grid search. We find that the observed and predicted coherency spectrogram match well. Specifically at 10 Hz (Figure 9c), the predicted and observed coherency demonstrate high consistency in both phase and amplitude for distance greater than 30 m. The corresponding phase velocity is 384.6 m/s and the attenuation coefficient is 0.0143/m. The extracted dispersion curve in the frequency range of $7-15$ Hz exhibits good consistency with that determined using the Frequency-Bessel method (Figure S12a). Additionally, the mean apparent Q-value estimated by the classical method, 5.33 (Figure S12b), falls within the uncertainty range of our results, 5.91 ± 0.73, validating the results of our method.

The developed method can be useful for monitoring temporal changes of velocity and Q-values at high resolution during processes of fault zone damage and healing using diffuse coda waves from aftershocks in large earthquake sequences. Other potential applications include monitoring sinkhole and landslide formation using diffuse waves generated by rail and road traffic with distributed acoustic sensing or dense nodal arrays.

5 Conclusions

We developed a frequency domain methodology for quantitative Evaluation of Diffuse Wavefield (EDWav). The method is applicable to single station's waveform and can

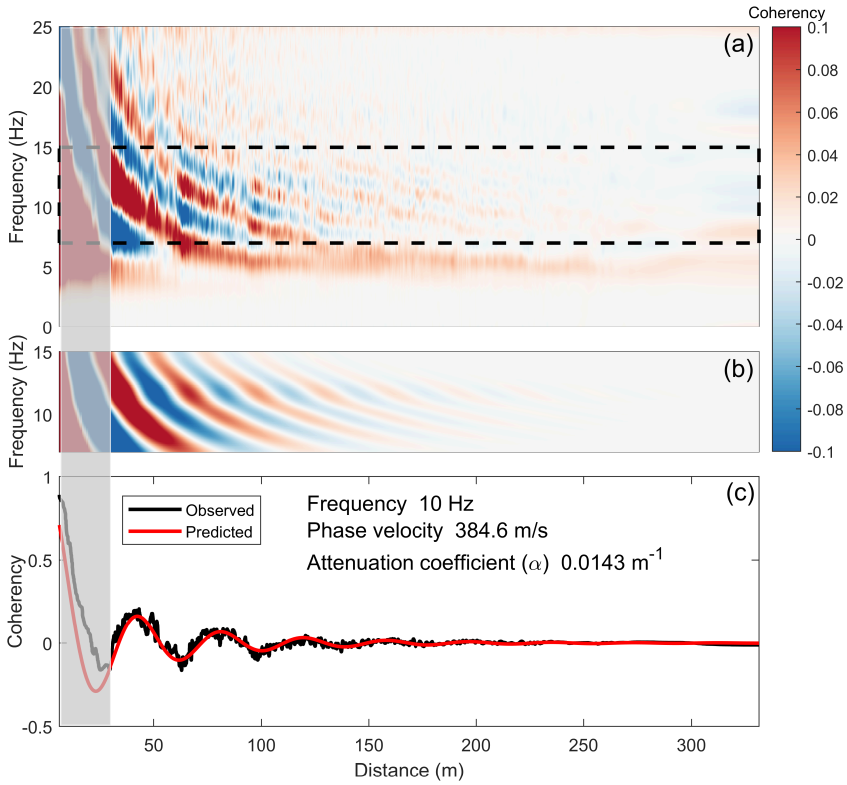

Figure 9. (a) The observed real part of coherency spectrogram of the sub-array (the red circles in Figure 1b) for one day data. The area enclosed by the black dashed box is the coherency for comparison. (b) The best fit prediction of the classical method through a grid search. (c) The observed and predicted coherency at 10 Hz. The coherencies at close distance (less than 30 m) covered by the the gray strip are not involved in residual calculation due to their irregular amplitudes.

effectively identify the diffuse segments in the continuous seismic waveform, thereby reducing data redundancy and improving computational efficiency while retaining reliable phase and amplitude. Our method allows to identify short-length (minute scale) diffuse waves and subsequently extract reliable dispersion curves and Q-values. Notably, the dispersion curve obtained through our approach using 60-second-long waveforms are consist with results derived from 1-day-long continuous recordings using conventional methods, which typically involve time and frequency domain normalization in data processing. As an example application, we use EDWav to separate ballistic and diffuse coda waves from a local M 2.2 earthquake recorded by a spatially dense array. Without performing amplitude-distorting normalization, the cross-correlation functions of the 60-second-long coda can robustly reconstruct the Rayleigh wave signals similar to continuous data used in conventional method. This demonstrates that short-duration diffuse waves with strong energy contain essential information for ANI, despite covering only a small portion of the continuous data. The methodology facilitates monitoring temporal changes of subsurface properties at high resolution based on the ambient seismic noise.

6 Open Research

The seismic data used in this paper can be obtained from the Data Management Center of the Incorporated Research Institutions for Seismology and Broadband Seismic Data Collection Center (Vernon et al., 2014) via `https://doi.org/10.7914/SN/ZG_2014`, and the IRIS Data Management Center via `https://ds.iris.edu/mda/9A/156/`. The Matlab and Python packages of EDWav are available through `https://github.com/yuanxzo/EDWav`.

Acknowledgments

We thank Dr. Xiaofeng Meng, Dr. Jing Li, Dr. Fan Xie, Dr. Tao Wang, and Dr. Jiajun Chong for insightful discussions. The manuscript benefited from constructive comments by Dr. Piero Poli and another anonymous reviewer, associated editor Dr. Nori Nakata, as well as editors Dr. Michael Bostock and Dr. Fenglin Niu. This study was supported by the Shenzhen Natural Science Foundation (No. 20220815100238003), Shenzhen Science and Technology Program (No. KQTD20170810111725321), Shanghai Sheshan National Geophysical Observatory (No. SSKP202303), National Natural Science Foundation of China (No. U1901602), Guangdong Provincial Key Laboratory of Geophysical High-resolution Imaging Technology (No. 2022B1212010002). The work of YBZ on methodology and interpretation was supported by the U.S. Department of Energy Office of Science (Award ED-SC0016520).

References

Aki, K., & Richards, P. G. (2002). *Quantitative Seismology* (2nd ed.). San Francisco: University Science Books.

Babadi, B., & Brown, E. N. (2014). A Review of Multitaper Spectral Analysis. *IEEE Transactions on Biomedical Engineering*, *61*(5), 1555–1564. doi: 10.1109/TBME.2014.2311996

Bensen, G. D., Ritzwoller, M. H., Barmin, M. P., Levshin, A. L., Lin, F., Moschetti, M. P., … Yang, Y. (2007). Processing seismic ambient noise data to obtain reliable broad-band surface wave dispersion measurements. *Geophysical Journal International*, *169*(3), 1239–1260. doi: 10.1111/j.1365-246X.2007.03374.x

Bensen, G. D., Ritzwoller, M. H., & Yang, Y. (2009). A 3-D shear velocity model of the crust and uppermost mantle beneath the United States from ambient seismic noise. *Geophysical Journal International*, *177*(3), 1177–1196. doi: 10.1111/j.1365-246X.2009.04125.x

Ben-Zion, Y., Vernon, F. L., Ozakin, Y., Zigone, D., Ross, Z. E., Meng, H., … Barklage, M. (2015). Basic data features and results from a spatially dense seismic array on the San Jacinto fault zone. *Geophysical Journal International*, *202*(1), 370–380. doi: 10.1093/gji/ggv142

Brenguier, F., Campillo, M., Takeda, T., Aoki, Y., Shapiro, N. M., Briand, X., … Miyake, H. (2014). Mapping pressurized volcanic fluids from induced crustal seismic velocity drops. *Science*, *345*(6192), 80–82. doi: 10.1126/science.1254073

Campillo, M., & Paul, A. (2003). Long-Range Correlations in the Diffuse Seismic Coda. *Science*, *299*(5606), 547–549. doi: 10.1126/science.1078551

Cheng, F., Xia, J., Xu, Y., Xu, Z., & Pan, Y. (2015). A new passive seismic method based on seismic interferometry and multichannel analysis of surface waves. *Journal of Applied Geophysics*, *117*, 126–135. doi: 10.1016/j.jappgeo.2015.04.005

Diaz, J., Ruiz, M., Udina, M., Polls, F., Martí, D., & Bech, J. (2023). Monitoring storm evolution using a high-density seismic network. *Scientific Reports*, *13*(1), 1853. doi: 10.1038/s41598-023-28902-8

Dziewonski, A. M., & Anderson, D. L. (1981). Preliminary reference Earth model. *Physics of the Earth and Planetary Interiors*, *25*(4), 297–356. doi: 10.1016/0031-9201(81)90046-7

Díaz, J., Ruiz, M., Sánchez-Pastor, P. S., & Romero, P. (2017). Urban Seismology: on the origin of earth vibrations within a city. *Scientific Reports*, *7*(1), 15296. doi: 10.1038/s41598-017-15499-y

Fan, W., McGuire, J. J., de Groot-Hedlin, C. D., Hedlin, M. A. H., Coats, S., & Fiedler, J. W. (2019). Stormquakes. *Geophysical Research Letters*, *46*(22), 12909–12918. doi: 10.1029/2019GL084217

Gu, N., Gao, J., Wang, B., Lu, R., Liu, B., Xu, X., & Zhang, H. (2022). Ambient noise tomography of local shallow structure of the southern segment of Tanlu fault zone at Suqian, eastern China. *Tectonophysics*, *825*, 229234. doi: 10.1016/j.tecto.2022.229234

Gu, N., Wang, K., Gao, J., Ding, N., Yao, H., & Zhang, H. (2019). Shallow Crustal Structure of the Tanlu Fault Zone Near Chao Lake in Eastern China by Direct Surface Wave Tomography from Local Dense Array Ambient Noise Analysis. *Pure and Applied Geophysics*, *176*(3), 1193–1206. doi: 10.1007/s00024-018-2041-4

Gutenberg, B., & Richter, C. F. (1944). Frequency of earthquakes in California. *Bulletin of the Seismological Society of America*, *34*(4), 185–188. doi: 10.1785/BSSA0340040185

Hennino, R., Trégourès, N., Shapiro, N. M., Margerin, L., Campillo, M., van Tiggelen, B. A., & Weaver, R. L. (2001). Observation of Equipartition of Seismic Waves. *Physical Review Letters*, *86*(15), 3447–3450. doi: 10.1103/PhysRevLett.86.3447

Hillers, G., Roux, P., Campillo, M., & Ben-Zion, Y. (2016). Focal spot imaging based on zero lag cross-correlation amplitude fields: Application to dense array data at the San Jacinto fault zone. *Journal of Geophysical Research: Solid Earth*, *121*(11), 8048–8067. doi: 10.1002/2016JB013014

Inbal, A., Cristea-Platon, T., Ampuero, J., Hillers, G., Agnew, D., & Hough, S. E. (2018). Sources of Long-Range Anthropogenic Noise in Southern California and Implications for Tectonic Tremor Detection. *Bulletin of the Seismological Society of America*. doi: 10.1785/0120180130

Johnson, C. W., Ben-Zion, Y., Meng, H., & Vernon, F. (2020). Identifying Different Classes of Seismic Noise Signals Using Unsupervised Learning. *Geophysical Research Letters*, *47*(15), e2020GL088353. doi: 10.1029/2020GL088353

Kuvshinov, A., & Olsen, N. (2006). A global model of mantle conductivity derived from 5 years of CHAMP, Ørsted, and SAC-C magnetic data. *Geophysical Research Letters*, *33*(18). doi: 10.1029/2006GL027083

Kuvshinov, A. V. (2008). 3-D Global Induction in the Oceans and Solid Earth: Recent Progress in Modeling Magnetic and Electric Fields from Sources of Magnetospheric, Ionospheric and Oceanic Origin. *Surveys in Geophysics*, *29*(2), 139–186. doi: 10.1007/s10712-008-9045-z

Li, Z., Zhou, J., Wu, G., Wang, J., Zhang, G., Dong, S., … Chen, X. (2021). CC-FJpy: A Python Package for Extracting Overtone Surface-Wave Dispersion from Seismic Ambient-Noise Cross Correlation. *Seismological Research Letters*, *92*(5), 3179–3186. doi: 10.1785/0220210042

Lin, F.-C., Li, D., Clayton, R. W., & Hollis, D. (2013). High-resolution 3D shallow crustal structure in Long Beach, California: Application of ambient noise tomography on a dense seismic array. *GEOPHYSICS*, *78*(4), Q45–Q56. doi: 10.1190/geo2012-0453.1

Lin, F.-C., Ritzwoller, M. H., Townend, J., Bannister, S., & Savage, M. K. (2007). Ambient noise Rayleigh wave tomography of New Zealand. *Geophysical Journal International*, *170*(2), 649–666. doi: 10.1111/j.1365-246X.2007.03414.x

Liu, Q., Feng, X., Liu, C., Zhang, M., Tian, Y., & Hou, H. (2022). Metallic mineral exploration by using ambient noise tomography in Ashele copper mine, Xinjiang, China. *Geophysics*, *87*(3), B221–B231. doi: 10.1190/geo2020-0923.1

Liu, X., & Ben-Zion, Y. (2016). Estimating correlations of neighbouring frequencies in ambient seismic noise. *Geophysical Journal International*, *206*(2), 1065–1075. doi: 10.1093/gji/ggw196

Lobkis, O. I., & Weaver, R. L. (2001). On the emergence of the Green's function in the correlations of a diffuse field. *The Journal of the Acoustical Society of America*, *110*(6), 3011–3017. doi: 10.1121/1.1417528

Maeda, T., Sato, H., & Ohtake, M. (2006). Constituents of Vertical-component Coda Waves at Long Periods. *pure and applied geophysics*, *163*(2-3), 549–566. doi: 10.1007/s00024-005-0031-9

Magrini, F., & Boschi, L. (2021). Surface-Wave Attenuation From Seismic Ambient Noise: Numerical Validation and Application. *Journal of Geophysical Research: Solid Earth*, *126*(1), e2020JB019865. doi: 10.1029/2020JB019865

Makus, P., Sens-Schönfelder, C., Illien, L., Walter, T. R., Yates, A., & Tilmann, F. (2023). Deciphering the Whisper of Volcanoes: Monitoring Velocity Changes at Kamchatka's Klyuchevskoy Group With Fluctuating Noise Fields. *Journal of Geophysical Research: Solid Earth*, *128*(4), e2022JB025738. doi: 10.1029/2022JB025738

Margerin, L., Campillo, M., Van Tiggelen, B. A., & Hennino, R. (2009). Energy partition of seismic coda waves in layered media: Theory and application to Pinyon Flats Observatory. *Geophysical Journal International*, *177*(2), 571–585. doi: 10.1111/j.1365-246X.2008.04068.x

Meng, H., & Ben-Zion, Y. (2018). Characteristics of Airplanes and Helicopters Recorded by a Dense Seismic Array Near Anza California. *Journal of Geophysical Research: Solid Earth*, *123*(6), 4783–4797. doi: 10.1029/2017JB015240

Meng, H., Ben-Zion, Y., & Johnson, C. W. (2019). Detection of random noise and anatomy of continuous seismic waveforms in dense array data near Anza California. *Geophysical Journal International*, *219*(3), 1463–1473. doi: 10.1093/gji/ggz349

Meng, H., Ben-Zion, Y., & Johnson, C. W. (2021). Analysis of Seismic Signals Generated by Vehicle Traffic with Application to Derivation of Subsurface Q-Values. *Seismological Research Letters*, *92*(4), 2354–2363. doi: 10.1785/0220200457

Mordret, A., Roux, P., Boué, P., & Ben-Zion, Y. (2019). Shallow three-dimensional structure of the San Jacinto fault zone revealed from ambient noise imaging with a dense seismic array. *Geophysical Journal International*, *216*(2), 896–905. doi: 10.1093/gji/ggy464

Nolet, G. (1977). The Upper Mantle under Western Europe Inferred from the Dis-

persion of Rayleigh Modes. *Journal of Geophysics*, *43*(1), 265–285.
Obermann, A., Kraft, T., Larose, E., & Wiemer, S. (2015). Potential of ambient seismic noise techniques to monitor the St. Gallen geothermal site (Switzerland). *Journal of Geophysical Research: Solid Earth*, *120*(6), 4301–4316. doi: 10.1002/2014JB011817
Obermann, A., Planès, T., Larose, E., & Campillo, M. (2019). 4-D Imaging of Subsurface Changes with Coda Waves: Numerical Studies of 3-D Combined Sensitivity Kernels and Applications to the Mw 7.9, 2008 Wenchuan Earthquake. *Pure and Applied Geophysics*, *176*(3), 1243–1254. doi: 10.1007/s00024-018-2014-7
Olivier, G., Brenguier, F., Campillo, M., Lynch, R., & Roux, P. (2015). Body-wave reconstruction from ambient seismic noise correlations in an underground mine. *Geophysics*, *80*(3), KS11–KS25. doi: 10.1190/geo2014-0299.1
Park, J., Lindberg, C. R., & Vernon, F. L. (1987). Multitaper spectral analysis of high-frequency seismograms. *Journal of Geophysical Research*, *92*(B12), 12675. doi: 10.1029/JB092iB12p12675
Paul, A., Campillo, M., Margerin, L., Larose, E., & Derode, A. (2005). Empirical synthesis of time-asymmetrical Green functions from the correlation of coda waves. *Journal of Geophysical Research: Solid Earth*, *110*(B8). doi: 10.1029/2004JB003521
Pedersen, H. A., Mattern, F., Poli, P., & Stehly, L. (2023). Imaging with seismic noise: improving extraction of body wave phases from the deep Earth through selective stacking based on H/V ratios. *Geophysical Journal International*, *232*(2), 1455–1467. doi: 10.1093/gji/ggac388
Planès, T., Obermann, A., Antunes, V., & Lupi, M. (2020). Ambient-noise tomography of the Greater Geneva Basin in a geothermal exploration context. *Geophysical Journal International*, *220*(1), 370–383. doi: 10.1093/gji/ggz457
Poli, P., Campillo, M., & De Hoop, M. (2017). Analysis of intermediate period correlations of coda from deep earthquakes. *Earth and Planetary Science Letters*, *477*, 147–155. doi: 10.1016/j.epsl.2017.08.026
Poli, P., Campillo, M., Pedersen, H., & LAPNET Working Group. (2012). Body-Wave Imaging of Earth's Mantle Discontinuities from Ambient Seismic Noise. *Science*, *338*(6110), 1063–1065. doi: 10.1126/science.1228194
Prieto, G. A., & Beroza, G. C. (2008). Earthquake ground motion prediction using the ambient seismic field. *Geophysical Research Letters*, *35*(14). doi: 10.1029/2008GL034428
Prieto, G. A., Denolle, M., Lawrence, J. F., & Beroza, G. C. (2011). On amplitude information carried by the ambient seismic field. *Nouveaux développements de l'imagerie et du suivi temporel à partir du bruit sismique*, *343*(8), 600–614. doi: 10.1016/j.crte.2011.03.006
Prieto, G. A., Lawrence, J. F., & Beroza, G. C. (2009). Anelastic Earth structure from the coherency of the ambient seismic field. *Journal of Geophysical Research*, *114*(B7), B07303. doi: 10.1029/2008JB006067
Prieto, G. A., Parker, R. L., Thomson, D. J., Vernon, F. L., & Graham, R. L. (2007). Reducing the bias of multitaper spectrum estimates: Reducing the bias of multitaper spectrum estimates. *Geophysical Journal International*, *171*(3), 1269–1281. doi: 10.1111/j.1365-246X.2007.03592.x
Qiu, H., Hillers, G., & Ben-Zion, Y. (2020). Temporal changes of seismic velocities in the San Jacinto Fault zone associated with the 2016 Mw 5.2 Borrego Springs earthquake. *Geophysical Journal International*, *220*(3), 1536–1554. doi: 10.1093/gji/ggz538
Riedel, K., & Sidorenko, A. (1995). Minimum bias multiple taper spectral estimation. *IEEE Transactions on Signal Processing*, *43*(1), 188–195. doi: 10.1109/78.365298
Ritzwoller, M. H., Lin, F.-C., & Shen, W. (2011). Ambient noise tomography with

a large seismic array. *Comptes Rendus Geoscience*, *343*(8), 558–570. doi: 10.1016/j.crte.2011.03.007

Robert, P., & Escoufier, Y. (1976). A Unifying Tool for Linear Multivariate Statistical Methods: The RV- Coefficient. *Applied Statistics*, *25*(3), 257. doi: 10.2307/2347233

Ross, Z. E., Trugman, D. T., Hauksson, E., & Shearer, P. M. (2019). Searching for hidden earthquakes in Southern California. *Science*, *364*(6442), 767–771. (Publisher: American Association for the Advancement of Science) doi: 10.1126/science.aaw6888

Roux, P., Moreau, L., Lecointre, A., Hillers, G., Campillo, M., Ben-Zion, Y., … Vernon, F. (2016). A methodological approach towards high-resolution surface wave imaging of the San Jacinto Fault Zone using ambient-noise recordings at a spatially dense array. *Geophysical Journal International*, *206*(2), 980–992. doi: 10.1093/gji/ggw193

Schimmel, M., Stutzmann, E., & Gallart, J. (2011). Using instantaneous phase coherence for signal extraction from ambient noise data at a local to a global scale. *Geophysical Journal International*, *184*(1), 494–506. doi: 10.1111/j.1365-246X.2010.04861.x

Seats, K. J., Lawrence, J. F., & Prieto, G. A. (2012). Improved ambient noise correlation functions using Welch's method. *Geophysical Journal International*, *188*(2), 513–523. doi: 10.1111/j.1365-246X.2011.05263.x

Sens-Schönfelder, C., Snieder, R., & Stähler, S. C. (2015). The lack of equipartitioning in global body wave coda. *Geophysical Research Letters*, *42*(18), 7483–7489. doi: 10.1002/2015GL065108

Shapiro, N. M., & Campillo, M. (2004). Emergence of broadband Rayleigh waves from correlations of the ambient seismic noise. *Geophysical Research Letters*, *31*(7). doi: 10.1029/2004GL019491

Shapiro, N. M., Campillo, M., Stehly, L., & Ritzwoller, M. H. (2005). High-Resolution Surface-Wave Tomography from Ambient Seismic Noise. *Science*, *307*(5715), 1615–1618. doi: 10.1126/science.1108339

Shen, Y., Ren, Y., Gao, H., & Savage, B. (2012). An Improved Method to Extract Very-Broadband Empirical Green's Functions from Ambient Seismic Noise. *Bulletin of the Seismological Society of America*, *102*(4), 1872–1877. doi: 10.1785/0120120023

Simons, F. J., Zuber, M. T., & Korenaga, J. (2000). Isostatic response of the Australian lithosphere: Estimation of effective elastic thickness and anisotropy using multitaper spectral analysis. *Journal of Geophysical Research: Solid Earth*, *105*(B8), 19163–19184. doi: 10.1029/2000JB900157

Smilde, A. K., Kiers, H. A. L., Bijlsma, S., Rubingh, C. M., & van Erk, M. J. (2009). Matrix correlations for high-dimensional data: the modified RV-coefficient. *Bioinformatics*, *25*(3), 401–405. doi: 10.1093/bioinformatics/btn634

Snieder, R., Sánchez-Sesma, F. J., & Wapenaar, K. (2009). Field Fluctuations, Imaging with Backscattered Waves, a Generalized Energy Theorem, and the Optical Theorem. *SIAM Journal on Imaging Sciences*, *2*(2), 763–776. doi: 10.1137/08072913X

Sánchez-Sesma, F. J., Pérez-Ruiz, J. A., Luzón, F., Campillo, M., & Rodríguez-Castellanos, A. (2008). Diffuse fields in dynamic elasticity. *Special Issue on Selected Papers Presented at the International Symposium on Mechanical Waves in Solids - Volume 2*, *45*(5), 641–654. doi: 10.1016/j.wavemoti.2007.07.005

Sánchez-Sesma, F. J., Rodríguez, M., Iturrarán-Viveros, U., Luzón, F., Campillo, M., Margerin, L., … Rodríguez-Castellanos, A. (2011). A theory for microtremor H/V spectral ratio: application for a layered medium. *Geophysical Journal International*, *186*(1), 221–225. doi: 10.1111/j.1365-246X.2011.05064.x

Taner, M. T., Koehler, F., & Sheriff, R. E. (1979). Complex seismic trace analysis. *GEOPHYSICS*, *44*(6), 1041–1063. doi: 10.1190/1.1440994

Thomson, D. (1982). Spectrum estimation and harmonic analysis. *Proceedings of the IEEE*, *70*(9), 1055–1096. doi: 10.1109/PROC.1982.12433

Tian, D., Wei, S. S., Wang, W., & Wang, F. (2022). Stress Drops of Intermediate-Depth and Deep Earthquakes in the Tonga Slab. *Journal of Geophysical Research: Solid Earth*, *127*(10), e2022JB025109. doi: 10.1029/2022JB025109

Tkalčić, H., Phạm, T.-S., & Wang, S. (2020). The Earth's coda correlation wavefield: Rise of the new paradigm and recent advances. *Earth-Science Reviews*, *208*, 103285. doi: 10.1016/j.earscirev.2020.103285

Vernon, F., Ben-Zion, Y., & Hollis, D. (2014). *Sage Brush Flats Nodal Experiment* [Dataset]. International Federation of Digital Seismograph Networks. Other/Seismic Network. doi: 10.7914/SN/ZG_2014

Wang, J., Wu, G., & Chen, X. (2019). Frequency-Bessel Transform Method for Effective Imaging of Higher-Mode Rayleigh Dispersion Curves From Ambient Seismic Noise Data. *Journal of Geophysical Research: Solid Earth*, *124*(4), 3708–3723. doi: 10.1029/2018JB016595

Wang, Q.-Y., & Yao, H. (2020). Monitoring of velocity changes based on seismic ambient noise: A brief review and perspective. *Earth and Planetary Physics*, *4*(5), 532–542. doi: 10.26464/epp2020048

Wang, S., & Tkalčić, H. (2020). Seismic Event Coda-Correlation: Toward Global Coda-Correlation Tomography. *Journal of Geophysical Research: Solid Earth*, *125*(4). doi: 10.1029/2019JB018848

Weaver, R. L. (1982). On diffuse waves in solid media. *The Journal of the Acoustical Society of America*, *71*(6), 1608–1609. doi: 10.1121/1.387816

Weaver, R. L. (2005). Information from Seismic Noise. *Science*, *307*(5715), 1568–1569. doi: 10.1126/science.1110534

Weaver, R. L., & Lobkis, O. I. (2001). Ultrasonics without a Source: Thermal Fluctuation Correlations at MHz Frequencies. *Physical Review Letters*, *87*(13), 134301. doi: 10.1103/PhysRevLett.87.134301

Weaver, R. L., & Lobkis, O. I. (2004). Diffuse fields in open systems and the emergence of the Green's function (L). *The Journal of the Acoustical Society of America*, *116*(5), 2731–2734.

White, M. C. A., Ben-Zion, Y., & Vernon, F. L. (2019). A Detailed Earthquake Catalog for the San Jacinto Fault-Zone Region in Southern California. *Journal of Geophysical Research: Solid Earth*, *124*(7), 6908–6930. doi: 10.1029/2019JB017641

Xia, S., Zhang, C., & Cao, J. (2022). Ambient noise tomography for coral islands. *Engineering*. doi: 10.1016/j.eng.2021.09.022

Xia, X., Li, Z., Bao, F., Xie, J., Shi, Y., You, Q., & Chen, H. (2021). Sedimentary structure of the Sichuan Basin derived from seismic ambient noise tomography. *Geophysical Journal International*, *225*(1), 54–67. doi: 10.1093/gji/ggaa578

Xie, J., Yang, Y., & Luo, Y. (2020). Improving cross-correlations of ambient noise using an rms-ratio selection stacking method. *Geophysical Journal International*, *222*(2), 989–1002. doi: 10.1093/gji/ggaa232

Yang, Y., Ritzwoller, M. H., Levshin, A. L., & Shapiro, N. M. (2007). Ambient noise Rayleigh wave tomography across Europe. *Geophysical Journal International*, *168*(1), 259–274. doi: 10.1111/j.1365-246X.2006.03203.x

Yao, H., & Van Der Hilst, R. D. (2009). Analysis of ambient noise energy distribution and phase velocity bias in ambient noise tomography, with application to SE Tibet. *Geophysical Journal International*, *179*(2), 1113–1132. (Publisher: John Wiley & Sons, Ltd) doi: 10.1111/j.1365-246X.2009.04329.x

Yao, H., van der Hilst, R. D., & de Hoop, M. V. (2006). Surface-wave array tomography in SE Tibet from ambient seismic noise and two-station analysis - I. Phase velocity maps. *Geophysical Journal International*, *166*(2), 732–744. doi:

10.1111/j.1365-246X.2006.03028.x

Zhan, W., Pan, L., & Chen, X. (2020). A widespread mid-crustal low-velocity layer beneath Northeast China revealed by the multimodal inversion of Rayleigh waves from ambient seismic noise. *Journal of Asian Earth Sciences*, *196*, 104372. doi: 10.1016/j.jseaes.2020.104372

Zhang, H., Meng, H., & Ben-Zion, Y. (2023). Lateral Variations Across the Southern San Andreas Fault Zone Revealed From Analysis of Traffic Signals at a Dense Seismic Array. *Geophysical Research Letters*, *50*(14), e2023GL103759. doi: 10.1029/2023GL103759

JGR: Solid Earth

Supporting Information for

A Frequency Domain Methodology for Quantitative Evaluation of Diffuse Wavefield with Applications to Seismic Imaging

Bo Yang[1], Haoran Meng[1*], Ning Gu[1], Xin Liu[3], Xiaofei Chen[1, 2], and Yehuda Ben-Zion[4, 5]

[1] Department of Earth and Space Sciences, Southern University of Science and Technology, Shenzhen, 518055, China
[2] Guangdong Provincial Key Laboratory of Geophysical High-resolution Imaging Technology, Southern University of Science and Technology, Shenzhen, 518055, China
[3] Department of Earth Sciences, University of Hong Kong, Hong Kong, China
[4] Department of Earth Sciences, University of Southern California, Los Angeles, California, USA
[5] Southern California Earthquake Center, Los Angeles, California, USA

*Corresponding author: Haoran Meng, menghr@sustech.edu.cn

Contents of this file

Text S1 to S3
Figures S1 to S12

Introduction

This file contains 3 supporting text and 12 additional figures for the results presented in the main manuscript:

Text S1 shows the derivation process of equations (7), (9), and (11).
Text S2 proves that the elements in conditions **A**, **B** and **C** are always greater than 0 and less than 1.
Text S3 shows the sRMS calculation equations applied to vectors and matrices.
Figure S1 shows the way how to obtain the appropriate scale factor.
Figure S2 is a diffuseness evaluation test for synthetic noise containing intensive single-frequency interferences.
Figure S3 is a diffuseness evaluation test for synthetic noise containing double the interferences intensity in Figure S2.
Figure S4 shows the complete three-component waveform recorded by node 156 on December 14, 2017, 00:02:20-00:03:20 (UTC time).

Figure S5 shows the evaluation results for earthquake late coda segments in Figure S4.
Figure S6 shows the evaluation results for earthquake ballistic wave segments in Figure S4.
Figure S7 shows the evaluation results of a car event coda.
Figure S8 is an examination of anatomical results of continuous seismic waveforms proposed by Meng et al. (2019).
Figure S9 shows how to achieve diffuse coda identification based on the differentiation in diffuseness proxies between the ballistic wave window and the coda wave window.
Figure S10 shows the energy distribution map and dispersion degree distribution map of the selected 60-second-long coda within the range of dense array deployment.
Figure S11 shows an example of randomly selected 60-second-long ambient noise cross-correlation functions and dispersion spectrum.
Figure S12 shows the dispersion curve and attenuation coefficient obtained by the classical method used by Prieto et al. (2009)

References

Meng, H., Ben-Zion, Y., & Johnson, C. W. (2019). Detection of random noise and anatomy of continuous seismic waveforms in dense array data near Anza California. Geophysical Journal International, 219(3), 1463–1473. doi: 10.1093/gji/ggz349

Prieto, G. A., Lawrence, J. F., & Beroza, G. C. (2009). Anelastic Earth structure from the coherency of the ambient seismic field. Journal of Geophysical Research, 114(B7), B07303. https://doi.org/10.1029/2008JB006067

Text S1.

According to Aki & Richards (2002), the vector wavefield $\boldsymbol{\psi}(\boldsymbol{r}, t)$ can be expressed as the superposition of normal modes,

$$\boldsymbol{\psi}(\boldsymbol{r}, t) = \mathrm{Re} \sum_n a_n \boldsymbol{u}^{(n)}(\boldsymbol{r}) e^{i\omega_n t}, \tag{S1}$$

where a_n denotes complex modal amplitudes, $\boldsymbol{u}^{(n)}(\boldsymbol{r})$ refers to vector normal mode eigenfunctions, $\boldsymbol{r}$ signifies the location vector, ω_n is angular frequency corresponding to the n-th mode, t denotes time, $i^2 = -1$, and $\mathrm{Re}[\cdot]$ signifies the real part of a complex function. When considering a single component, we project $\boldsymbol{\psi}(\boldsymbol{r}, t)$ in the direction of the unit vector $\hat{\boldsymbol{e}}$,

$$\begin{aligned} \psi(\boldsymbol{r}, t) &= \boldsymbol{\psi}(\boldsymbol{r}, t) \cdot \hat{\boldsymbol{e}} \\ &= \mathrm{Re} \sum_n a_n \left[\boldsymbol{u}^{(n)}(\boldsymbol{r}) \cdot \hat{\boldsymbol{e}}\right] e^{i\omega_n t} \\ &= \mathrm{Re} \sum_n a_n u^{(n)}(\boldsymbol{r}) e^{i\omega_n t}, \end{aligned} \tag{S2}$$

where $\hat{\boldsymbol{e}}$ could be either vertical or horizontal. Notably, as the modal amplitudes a_n are consistent across all three components, the derived conditions $\boldsymbol{A}$, $\boldsymbol{B}$, and $\boldsymbol{C}$, which are independent to the eigenfunctions, are universally applicable to all components. By adopting equation (5) of the revised manuscript, $\mathrm{E}\left[a_p\right] = 0$, $\mathrm{E}\left[a_p a_q\right] = 0$, and $\mathrm{E}\left[a_p a_q^*\right] = F\left(\omega_p\right)\delta_{pq}$ for a fully diffuse wavefield, the proof details are as follows.

$$\begin{aligned} \boldsymbol{A}\left(\boldsymbol{r}, \omega_p\right) &= \frac{\left|\mathrm{E}\left[\phi\left(\boldsymbol{r}, \omega_p\right)\right]\right|^2}{\mathrm{E}\left[\left|\phi\left(\boldsymbol{r}, \omega_p\right)\right|^2\right]} = \frac{\left|\mathrm{E}\left[a_p\right]\right|^2 \left|u^{(p)}(\boldsymbol{r})T\right|^2}{\mathrm{E}\left[\left|a_p\right|^2\right] \left|u^{(p)}(\boldsymbol{r})T\right|^2} \\ &= \frac{\left|\mathrm{E}\left[a_p\right]\right|^2}{\mathrm{E}\left[\left|a_p\right|^2\right]} = 0; \end{aligned} \tag{S3}$$

$$\begin{aligned} \boldsymbol{B}\left(\boldsymbol{r}, \omega_p, \omega_q\right) &= \frac{\left|\mathrm{E}\left[\phi\left(\boldsymbol{r}, \omega_p\right)\phi\left(\boldsymbol{r}, \omega_q\right)\right]\right|^2}{\mathrm{E}\left[\left|\phi\left(\boldsymbol{r}, \omega_p\right)\right|^2\right] \mathrm{E}\left[\left|\phi\left(\boldsymbol{r}, \omega_q\right)\right|^2\right]} \\ &= \frac{\left|\mathrm{E}\left[a_p a_q\right] u^{(p)}(\boldsymbol{r}) u^{(q)}(\boldsymbol{r}) T^2\right|^2}{\mathrm{E}\left[\left|a_p\right|^2\right] \mathrm{E}\left[\left|a_q\right|^2\right] \left|u^{(p)}(\boldsymbol{r})T\right|^2 \left|u^{(q)}(\boldsymbol{r})T\right|^2} \\ &= \frac{\left|\mathrm{E}\left[a_p a_q\right]\right|^2}{\mathrm{E}\left[\left|a_p\right|^2\right] \mathrm{E}\left[\left|a_q\right|^2\right]} = 0; \end{aligned} \tag{S4}$$

$$\begin{aligned} \boldsymbol{C}\left(\boldsymbol{r}, \omega_p, \omega_q\right) &= \frac{\left|\mathrm{E}\left[\phi\left(\boldsymbol{r}, \omega_p\right)\phi^*\left(\boldsymbol{r}, \omega_q\right)\right]\right|^2}{\mathrm{E}\left[\left|\phi\left(\boldsymbol{r}, \omega_p\right)\right|^2\right] \mathrm{E}\left[\left|\phi^*\left(\boldsymbol{r}, \omega_q\right)\right|^2\right]} \\ &= \frac{\left|\mathrm{E}\left[a_p a_q^*\right] u^{(p)}(\boldsymbol{r}) u^{(q)*}(\boldsymbol{r}) T^2\right|^2}{\mathrm{E}\left[\left|a_p\right|^2\right] \mathrm{E}\left[\left|a_q^*\right|^2\right] \left|u^{(p)}(\boldsymbol{r})T\right|^2 \left|u^{(q)*}(\boldsymbol{r})T\right|^2} \\ &= \frac{\left|\mathrm{E}\left[a_p a_q^*\right]\right|^2}{\mathrm{E}\left[\left|a_p\right|^2\right] \mathrm{E}\left[\left|a_q^*\right|^2\right]} = \delta_{pq}. \end{aligned} \tag{S5}$$

Text S2.

To prove inequalities (equations 11a-11c) in subsection 2.2, we can start by defining two random variables, X and Y, that are not completely zero. According to the non-negativity of the $|\mathrm{E}[XY]|^2$, $\mathrm{E}[|X|^2]$ and $\mathrm{E}[|Y|^2]$, we have

$$\frac{|\mathrm{E}[XY]|^2}{\mathrm{E}[|X|^2]\mathrm{E}[|Y|^2]} \geq 0. \tag{S6}$$

where $\mathrm{E}[\cdot]$ is the expectation operator and $|\cdot|$ is the absolute value operator. According to Jensen's inequality, that is, $f(\mathrm{E}[X]) \leq \mathrm{E}[f(X)]$, where $f(\cdot)$ is a convex function. When $f(\cdot)$ is $|\cdot|$, we have,

$$|\mathrm{E}[XY]|^2 \leq \mathrm{E}[|XY|]^2. \tag{S7}$$

Since $|XY| \leq |X||Y|$,

$$|\mathrm{E}[XY]|^2 \leq \mathrm{E}[|XY|]^2 \leq \mathrm{E}[|X||Y|]^2. \tag{S8}$$

Combining inequality (S1) and (S3), there is

$$0 \leq \frac{|\mathrm{E}[XY]|^2}{\mathrm{E}[|X|^2]\mathrm{E}[|Y|^2]} \leq \frac{\mathrm{E}[|X||Y|]^2}{\mathrm{E}[|X|^2]\mathrm{E}[|Y|^2]}. \tag{S9}$$

Defining a new random variable $Z = |X| - s|Y|$, where s is a scalar. We can choose s to be equal to $\frac{\mathrm{E}[|X||Y|]}{\mathrm{E}[|Y|^2]}$, which ensures that the expected value of Z^2 is non-negative:

$$\begin{aligned}\mathrm{E}[Z^2] = \mathrm{E}[(|X| - s|Y|)^2] &= \mathrm{E}[|X|^2] - 2s\mathrm{E}[|X||Y|] + s^2\mathrm{E}\left[|Y|^2\right] \\ &= \mathrm{E}[|X|^2] - 2\frac{\mathrm{E}[|X||Y|]^2}{\mathrm{E}[|Y|^2]} + \frac{\mathrm{E}[|X||Y|]^2}{\mathrm{E}[|Y|^2]} \\ &= \mathrm{E}[|X|^2] - \frac{\mathrm{E}[|X||Y|]^2}{\mathrm{E}[|Y|^2]} \geq 0. \end{aligned} \tag{S10}$$

Actually, that is the Cauchy-Schwarz Inequality. Multiplying both sides of this inequality by $1/\mathrm{E}[|X|^2]$ and rearranging terms, we obtain:

$$\frac{\mathrm{E}[|X||Y|]^2}{\mathrm{E}[|X|^2]\mathrm{E}[|Y|^2]} \leq 1. \tag{S11}$$

Combining inequality (S4) and (S6), there is

$$0 \leq \frac{|\mathrm{E}[XY]|^2}{\mathrm{E}[|X|^2]\mathrm{E}[|Y|^2]} \leq 1. \tag{S12}$$

Therefore, let X be equal to $\phi(\mathbf{r}, \omega_p)$ of the equation (6), $Y = 1$, and we can obtain

$$0 \leq A(\mathbf{r}, \omega_p) = \frac{|\mathrm{E}[\phi(\mathbf{r}, \omega_p)]|^2}{\mathrm{E}\left[\left|\phi(\mathbf{r}, \omega_p)\right|^2\right]} \leq 1; \tag{S13}$$

Next, let X and Y be equal to $\phi(\mathbf{r}, \omega_p)$ and $\phi(\mathbf{r}, \omega_q)$ of the equation (8), respectively, and we can obtain

$$0 \leq B(\mathbf{r}, \omega_p, \omega_q) = \frac{|\mathrm{E}[\phi(\mathbf{r}, \omega_p)\phi(\mathbf{r}, \omega_q)]|^2}{\mathrm{E}\left[\left|\phi(\mathbf{r}, \omega_p)\right|^2\right]\mathrm{E}\left[\left|\phi(\mathbf{r}, \omega_q)\right|^2\right]} \leq 1; \tag{S14}$$

Finally, let X and Y be equal to $\phi(\mathbf{r}, \omega_p)$ and $\phi^*(\mathbf{r}, \omega_q)$ of the equation (10), respectively, and we can obtain

$$0 \leq C(\mathbf{r}, \omega_p, \omega_q) = \frac{|\mathrm{E}[\phi(\mathbf{r}, \omega_p)\phi^*(\mathbf{r}, \omega_q)]|^2}{\mathrm{E}\left[\left|\phi(\mathbf{r}, \omega_p)\right|^2\right]\mathrm{E}\left[\left|\phi^*(\mathbf{r}, \omega_q)\right|^2\right]} \leq 1. \tag{S15}$$

Text S3.

The scale-dependent Root Mean Square (sRMS) function applied to vector cases is

$$P = \sqrt{\frac{\sum_{j=1}^{N}\left(w_j x_j\right)^2}{N}}, \tag{S16}$$

where $x_j = \left|A_j^{\mathrm{obs}} - A_j^{\mathrm{tar}}\right|$ is jth element of the absolute value of the residual of the observed and target of the condition $\mathbf{A}$ with size of $1 \times N$, w_j is the weight of x_j, and defined as

$$w_j = \left(\frac{1}{2s+1}\sum_{k=j-s}^{j+s} x_k\right)/\mathrm{mean}[\mathbf{x}], \tag{S17}$$

where s is the scale of the window $(2s+1)$ of the weight, $\mathbf{x}$ is the set of all x_j $(1 \leq j \leq N)$.

When sRMS function is applied to square matrix cases, such as condition $\mathbf{B}$ and $\mathbf{C}$, simple extensions to equations S11 and S12 are required. That is,

$$P = \sqrt{\frac{\sum_{j=1}^{N}\sum_{i=1}^{N}\left(w_{ij} x_{ij}\right)^2}{N^2}}, \tag{S18}$$

where $x_{ij} = \left|D_{ij}^{\mathrm{obs}} - D_{ij}^{\mathrm{tar}}\right|$ is ith row and jth column element of the absolute value of the residual of the observed and target of the square matrix $\mathbf{D}$ with N rows and N columns, w_{ij} is the weight of x_{ij}, and defined as

$$w_{ij} = \left(\frac{1}{(2s+1)^2}\sum_{l=j-s}^{j+s}\sum_{k=i-s}^{i+s} x_{kl}\right)/\mathrm{mean}[\mathbf{x}], \tag{S19}$$

where $\mathbf{x}$ is the set of all x_{ij} $(1 \leq i \leq N, 1 \leq j \leq N)$. When calculating the proxy of condition $\mathbf{B}$, let $\mathbf{D} = \mathbf{B}$, while for the case of condition $\mathbf{C}$, let $\mathbf{D} = \mathbf{C}$.

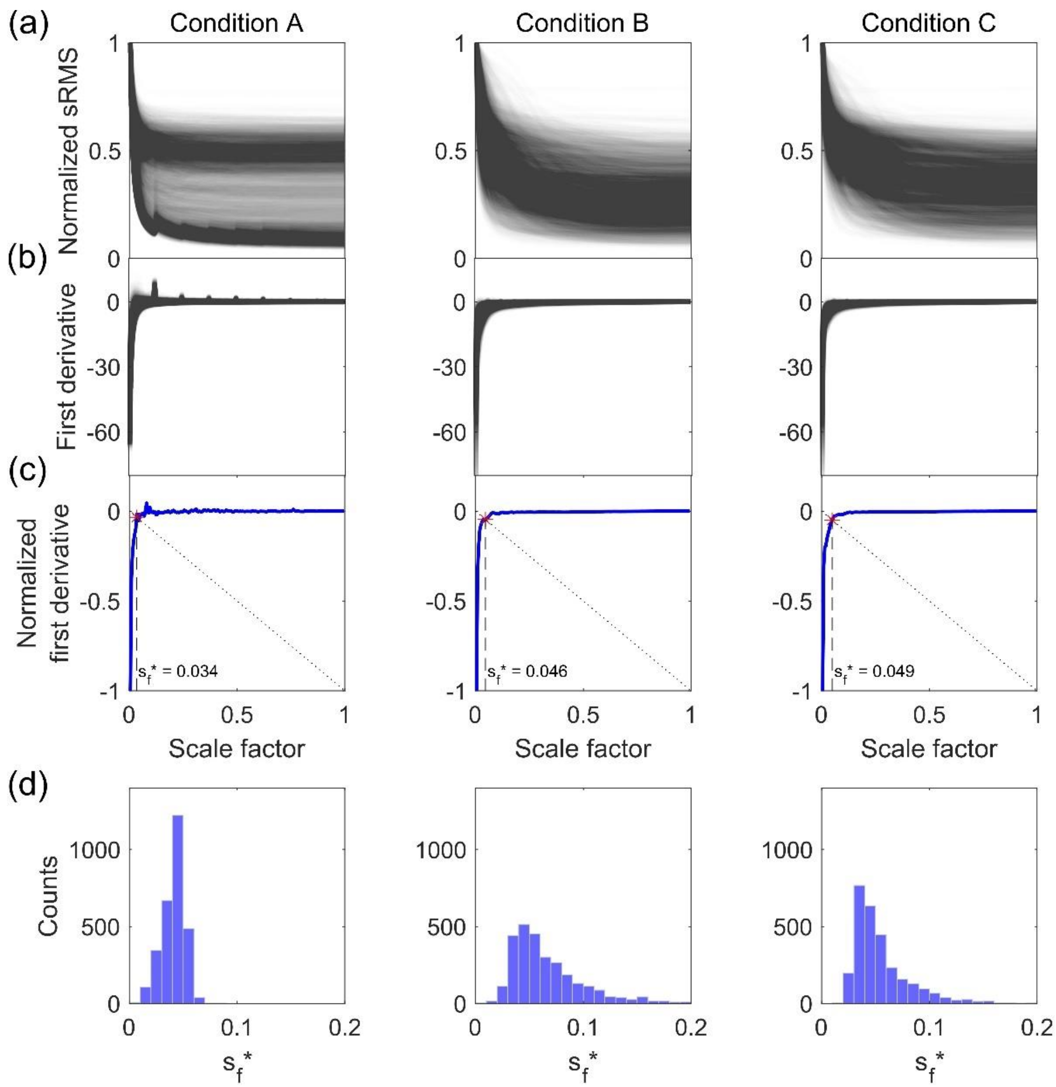

Figure S1. The determination of appropriate scale factor. From left to right, each column corresponds to the case of conditions **A**, **B** and **C**, respectively. (a) First row: plot of normalized sRMS with scale factor variation obtained by evaluating 2880 segment 60-second-long waveform data recorded by geophone R3010 (See Figure 1) from Julian day 131, 2014 to Julian day 132, 2014. (b) Second row: the first derivative of the 2880 curves in (a). (c) Third row: a result chosen at random from (b) and normalized (blue curve). The intersection (red star) of the blue curve and the auxiliary curve (black dashed line with a slope of -1 and passing through the origin) is considered by us as the corner point of the blue curve, and the appropriate scale factor ($\boldsymbol{s}_{\mathbf{f}}^{*}$) is determined by the abscissa of this corner point. (d) Fourth row: the statistical histogram of the abscissa of this corner points of the 2880 segment waveform data calculated by the approach in (c). The result shows that the $\boldsymbol{s}_{\mathbf{f}}^{*}$ of the 2880 segment different sample data for conditions **A**, **B** and **C** are most distributed in the intervals [0.04, 0.05], [0.04, 0.05], and [0.03, 0.04], respectively. These three intervals are very close to each other, all within the interval [0.03, 0.05], which means that choosing a $\boldsymbol{s}_{\mathbf{f}}^{*}$ from [0.03, 0.05] can be applied to the proxy calculation of conditions **A**, **B** and **C** at the same time. The consistency interval given by the 2880 samples also shows that it can be applied to the calculation of proxies in a broader range of data. Hence, in our paper, we adopt $\boldsymbol{s}_{\mathbf{f}}^{*} = \mathbf{0.05}$. Of course, the method for finding the corner point introduced above can also be performed independently for the data to be studied to obtain the specific $\boldsymbol{s}_{\mathbf{f}}^{*}$.

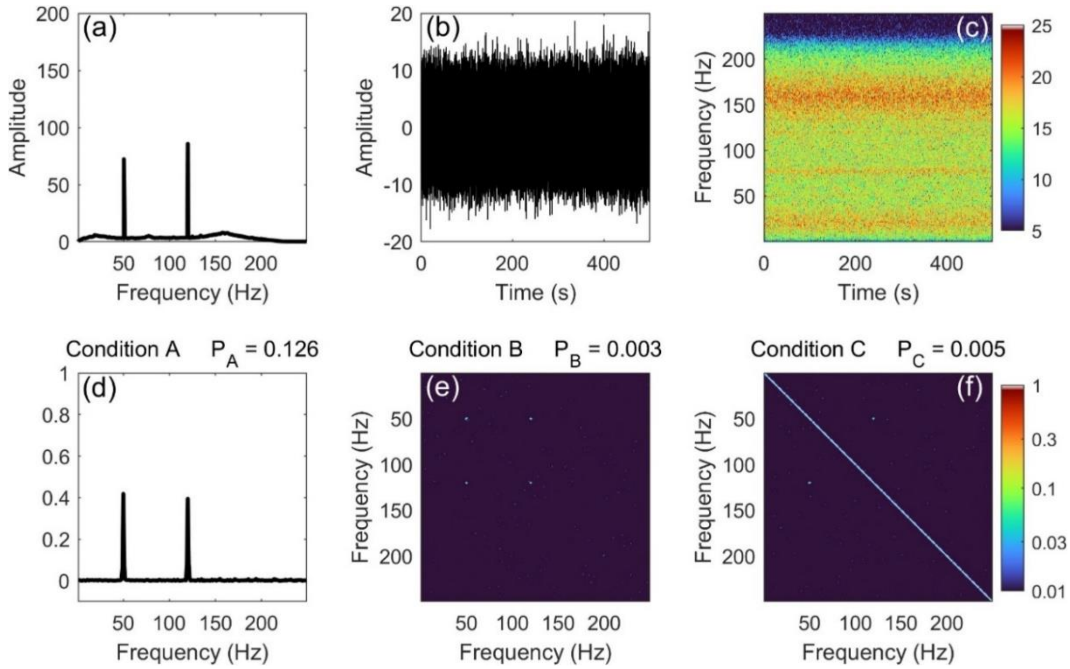

Figure S2. (a) Amplitude spectrum after adding 50 Hz and 120 Hz single frequency interferences to the data in Fig. 2b. (b) Synthetic waveform using the amplitude spectrum in (a). (c) The spectrogram of the synthetic waveform. (d-f) The conditions A, B and C of the synthetic waveform in (b).

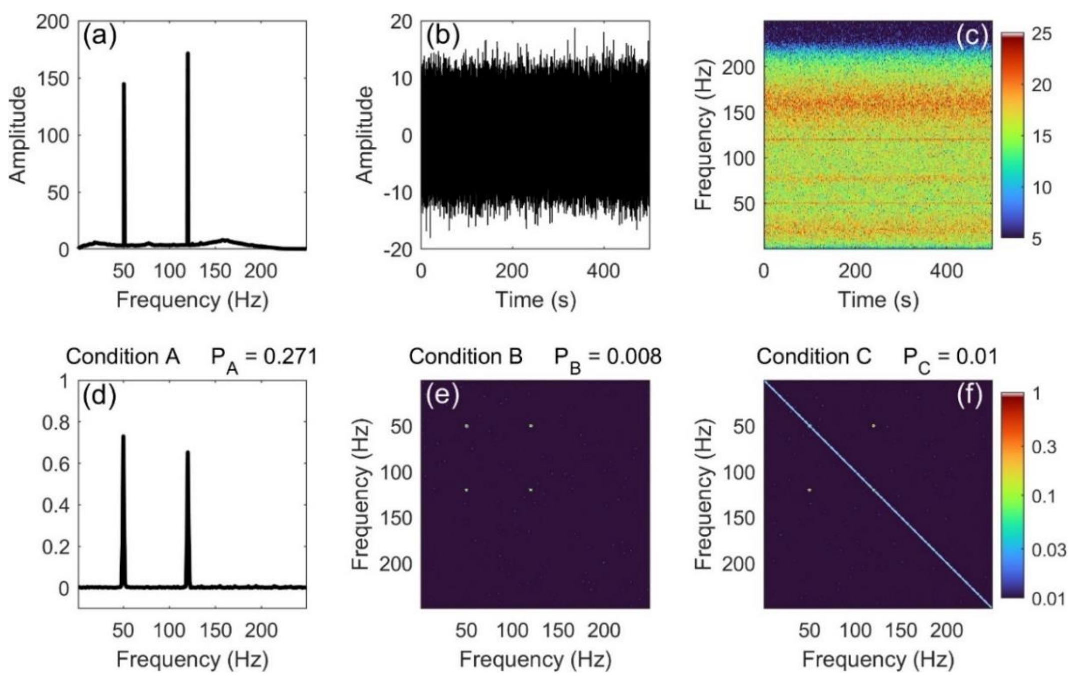

Figure S3. Similar to Figure S2, but the evaluation of waveforms synthesized with amplitudes containing double the interferences intensity in Figure S2.

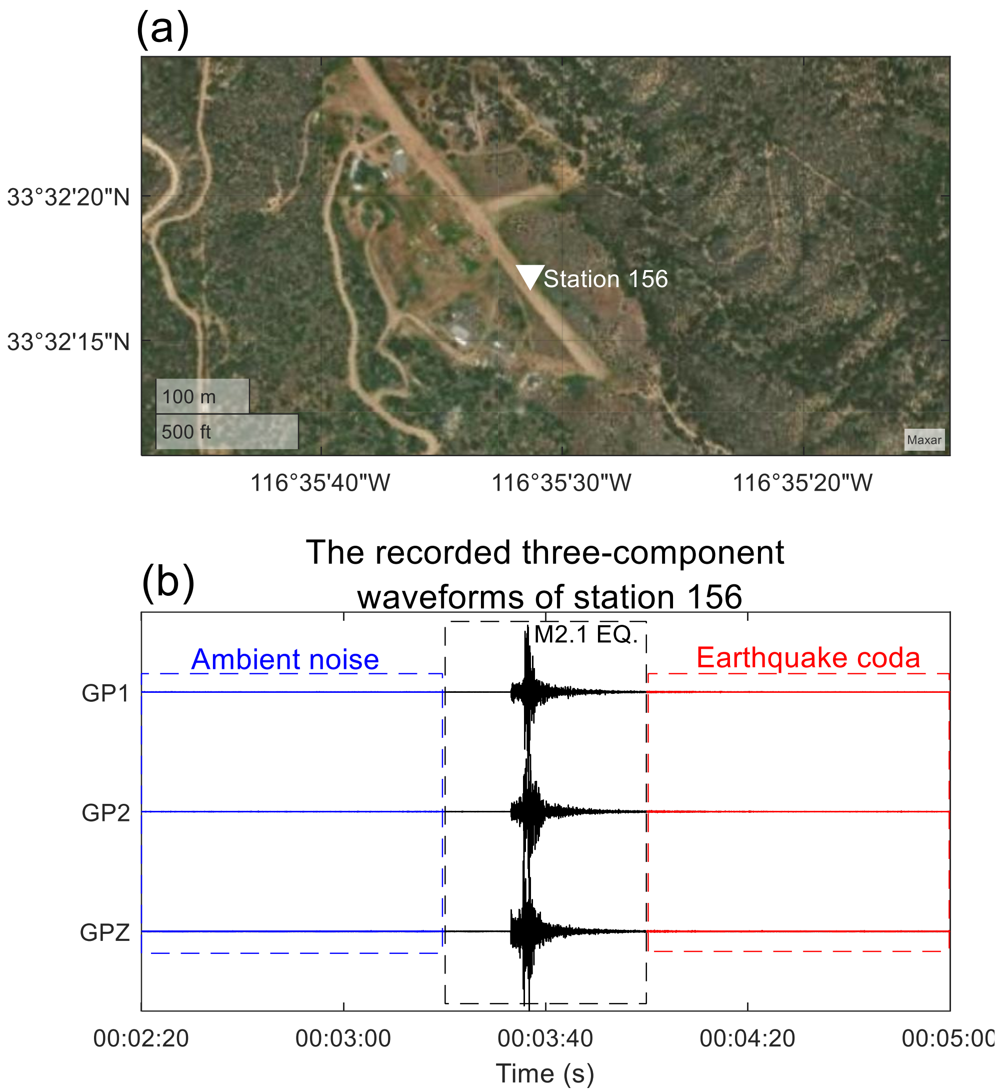

Figure S4. (a) The location satellite map of node 156 of 9A network. (b) The three-component waveforms recorded by node 156 on December 14, 2017, 00:02:20-00:05:00 UTC time. The 60-second-long ambient noise segments enclosed by the blue box corresponds to Figure 3 of the paper manuscript.

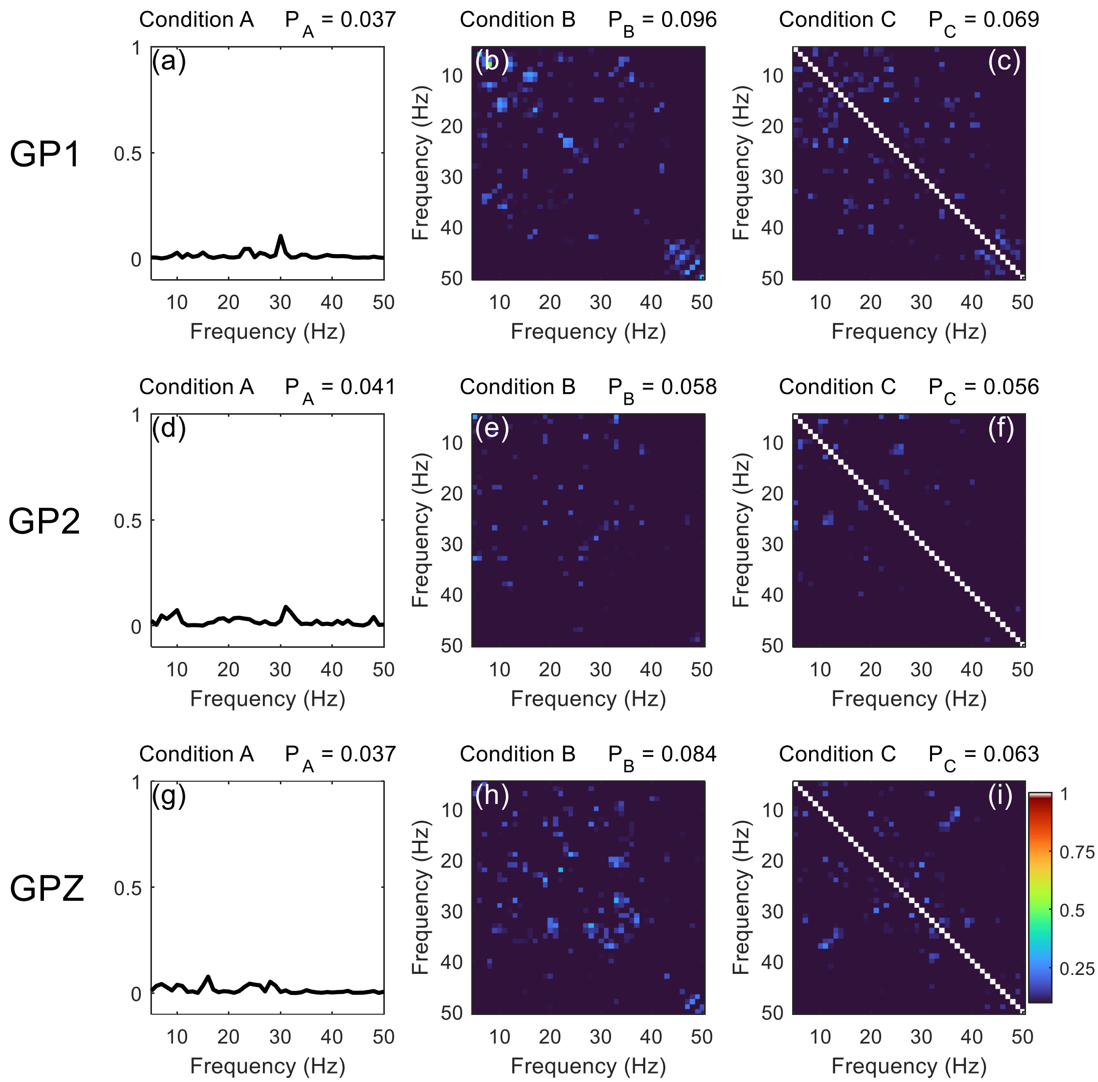

Figure S5. The evaluation results for earthquake late coda segments (red box in Figure S4) of the three-component waveforms recorded by station 156. The first and second rows correspond to the results of the horizontal components GP1 and GP2, respectively, while the third row correspond to the vertical component GPZ.

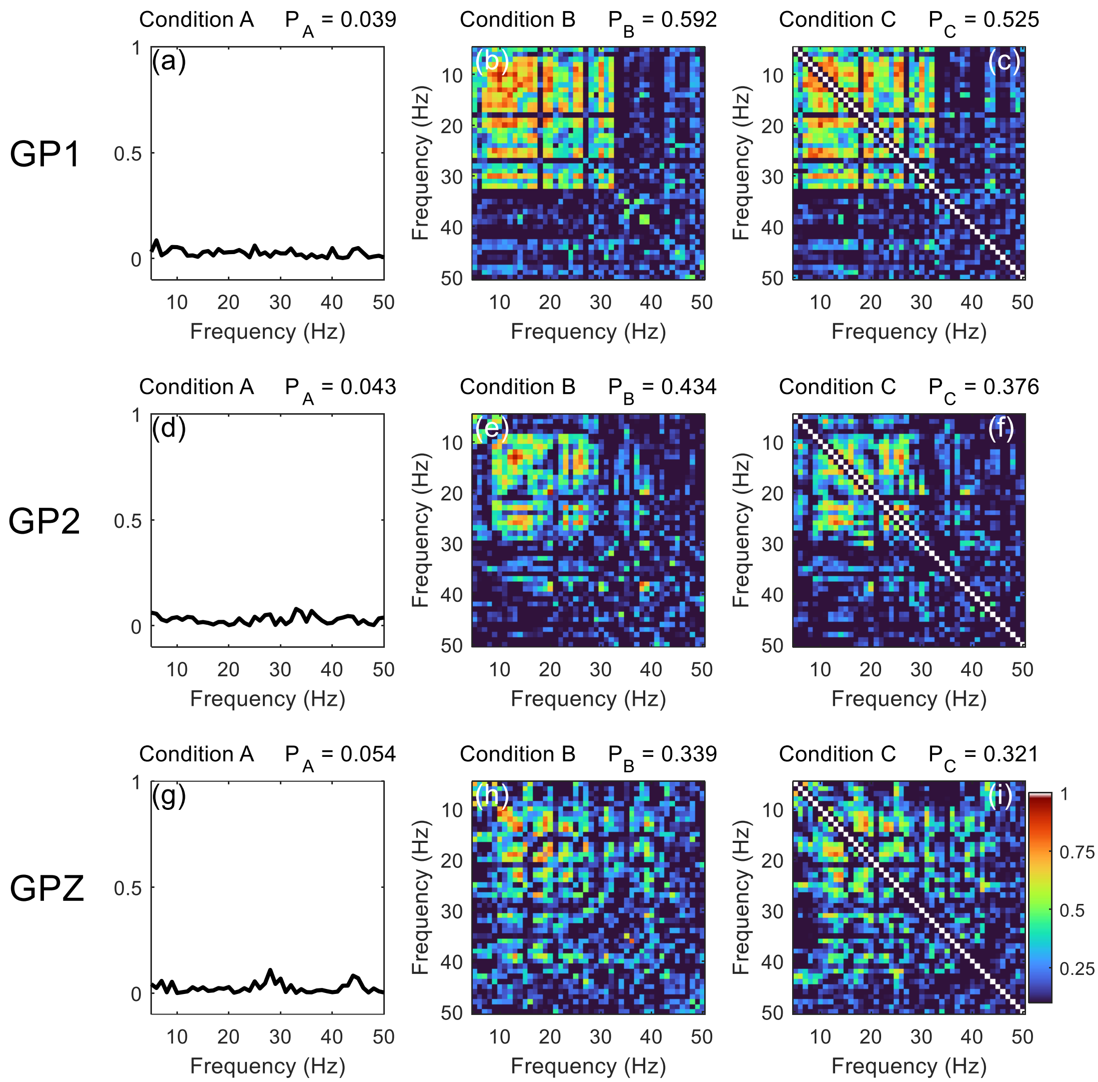

Figure S6. The evaluation results for earthquake ballistic wave segments (black box in Figure S4) of the three-component waveforms recorded by station 156. The first and second rows correspond to the results of the horizontal components GP1 and GP2, respectively, while the third row correspond to the vertical component GPZ.

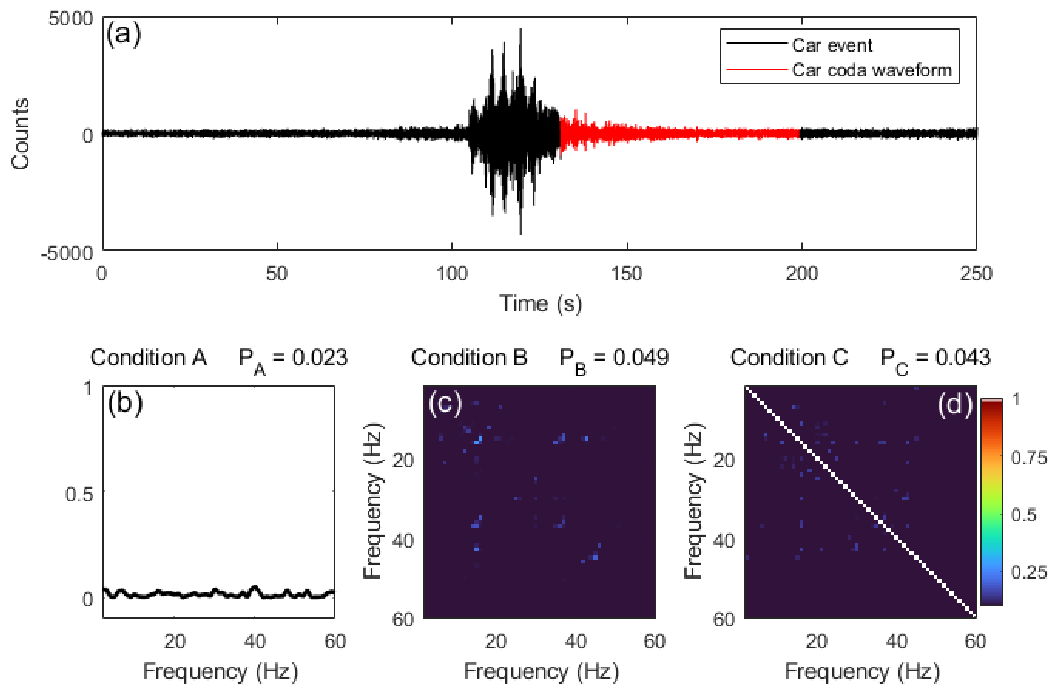

Figure S7. The evaluation results for a car event coda. Due to the fact that within the 60 Hz range, condition A is close to a zero vector, condition B is close to a zero matrix, and condition C is close to an identity matrix, it can be considered that the car coda wave is sufficiently diffused in that frequency band.

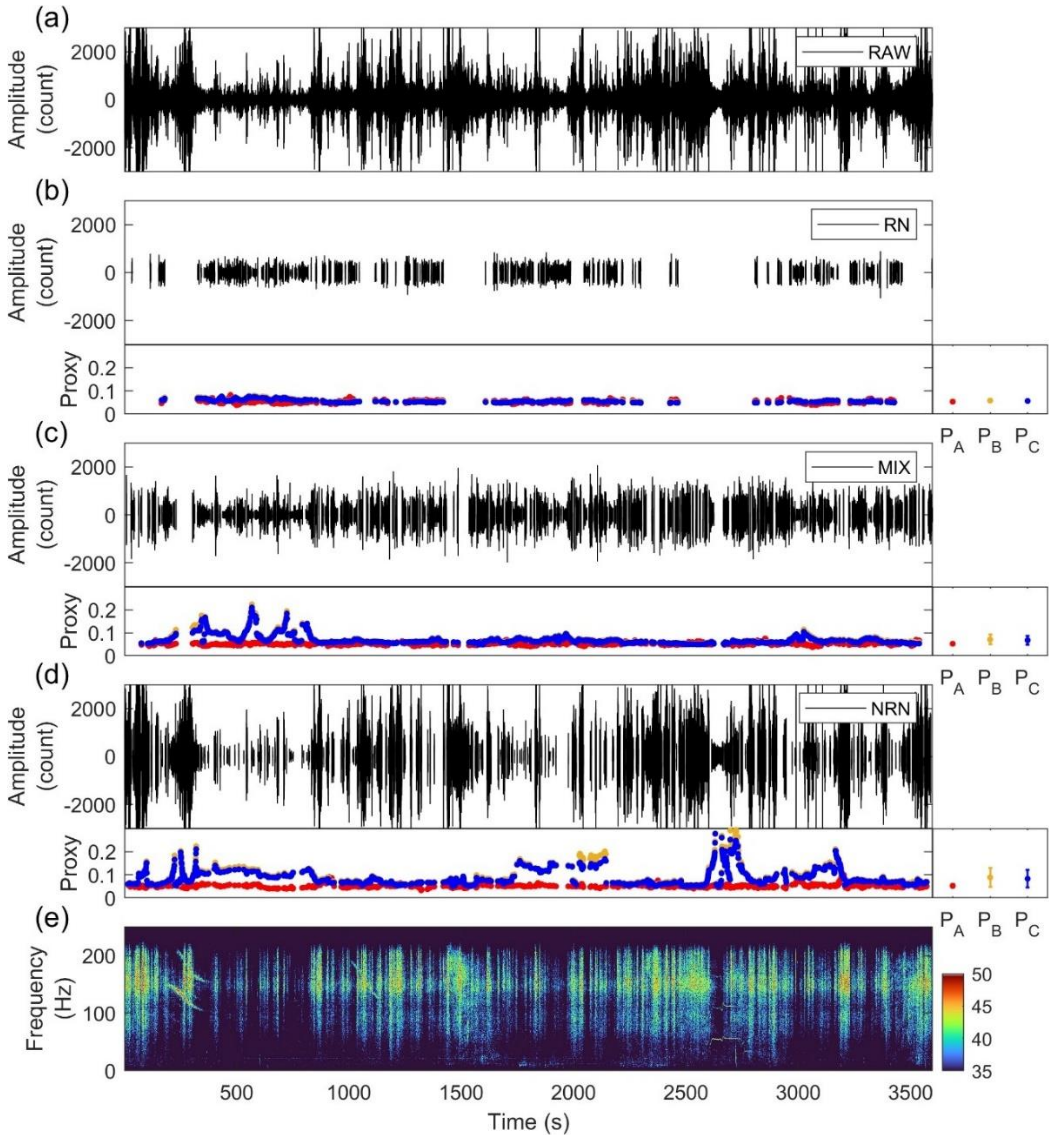

Figure S8. Examination of anatomical results of continuous seismic waveforms proposed by Meng et al. (2019). (a) The raw continuous seismic waveforms recorded by geophone R3010 on Julian day 146, 2014 from 14:00 to 15:00 (local time). (e) Corresponding spectrogram of the waveform in (a). The upper panel of (b), (c) and (d) show the RN, MIX and NRN signals separated from waveform in (a), respectively. The degree of diffuseness of these signals are evaluated in a sliding window of length 30 s with an overlap of 29 s, and the results are presented in the lower panels of (b), (c) and (d), respectively. The red, orange and blue points are the evaluation proxies corresponding to the conditions **A**, **B** and **C**, respectively. The bottom right panels of (b), (c), and (d) show the mean of the evaluation proxies with standard deviations.

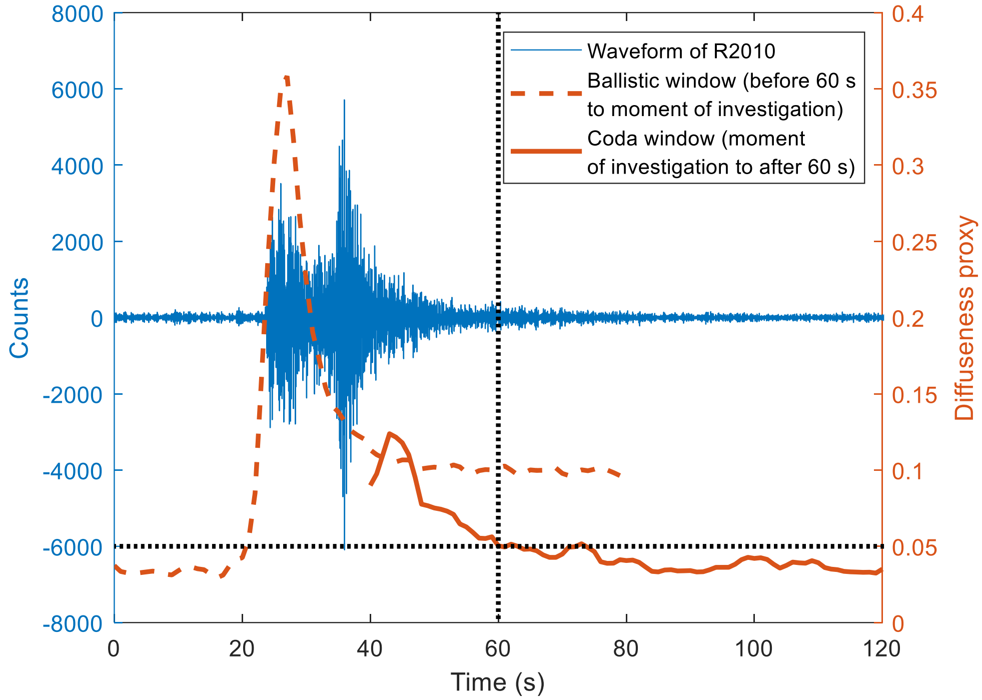

Figure S9. The variation of the diffuseness proxy (The diffuseness proxy here refers to the mean value of $\boldsymbol{P_A}$, $\boldsymbol{P_B}$ and $\boldsymbol{P_C}$) of the two windows as they slide with the moment of investigation. The first sliding window is referred to as the "ballistic window", and the last window is referred to as the "coda window". The intersection point between the two windows is referred to as the moment of investigation. We can observe that during the period of 40 seconds to 80 seconds when both windows coexist, the diffuseness proxy of the "ballistic window" tends to stabilize, while the diffuseness proxy of the "coda window" continues to decrease. As it decreases, the difference between the two gradually increases. Until the 60 seconds moment, the diffuseness proxy of the "coda window" is below 0.05 for the first time, which can be considered as sufficient diffusive. Therefore, the last 60 seconds waveform at this moment is defined as the selected diffuse coda wave, while the 60 seconds waveform before this moment is defined as the non-diffuse ballistic wave we use for comparison.

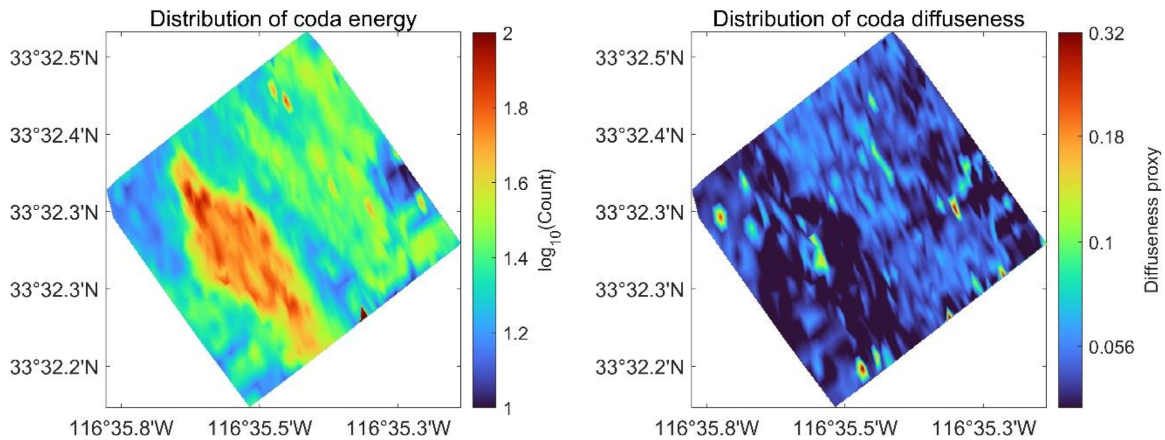

Figure S10. (a) The energy distribution map of the coda wave of the local M 2.2 Earthquake recorded by the SGB site stations in the 4-21 Hz frequency band range. This energy here refers to the average count of the selected 60-second-long coda wave. (b) The distribution map of the diffuseness of these coda waves selected by our method.

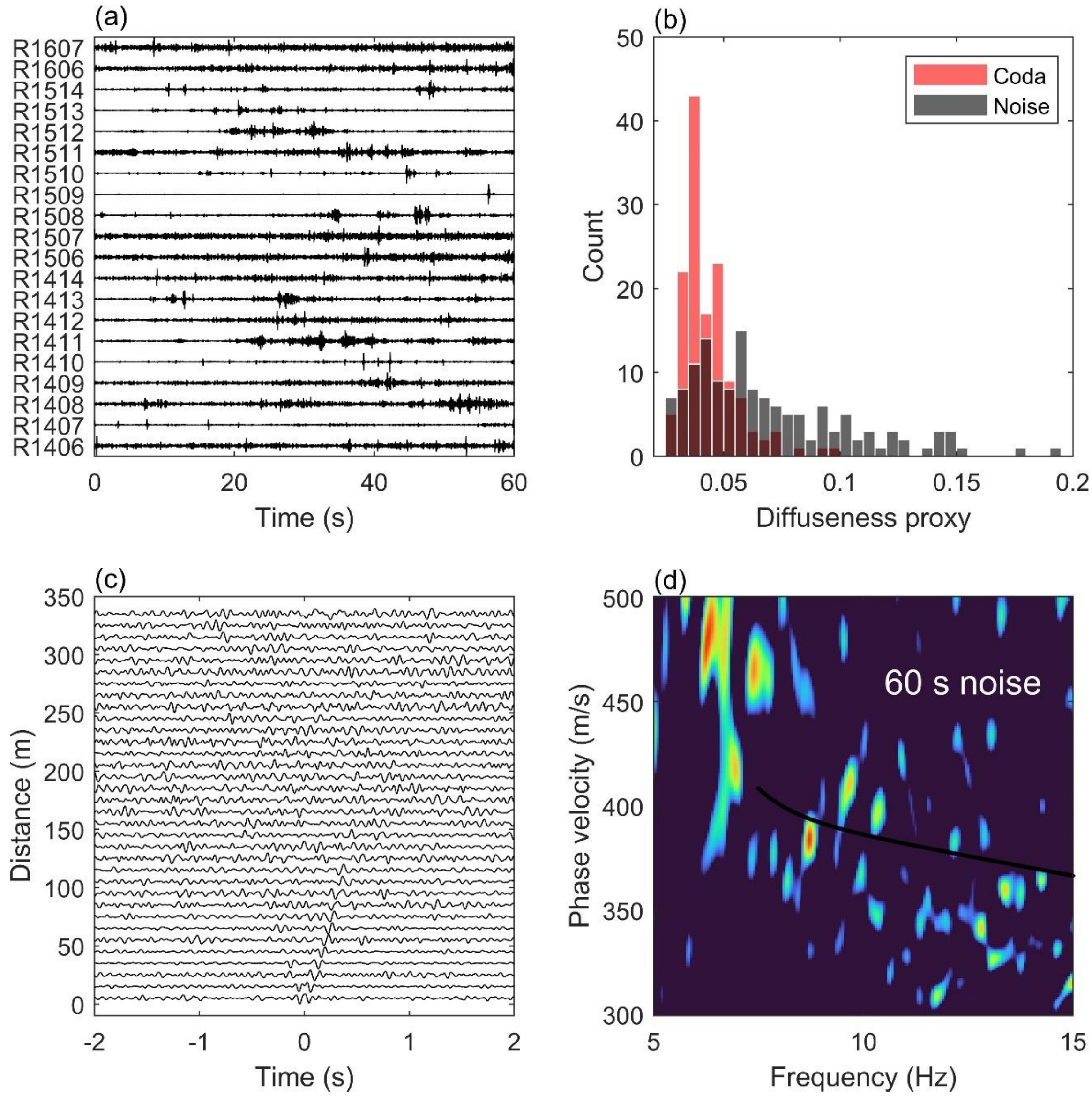

Figure S11. Ambient noise cross-correlation and dispersion spectrum. The 60-second-long ambient noises are randomly cut from the Julian day 131, 2014. (a) The 4-21Hz bandpass filtered waveforms recorded by some stations of the analyzed array. (b) The statistical histogram of diffuseness proxies of the ambient noises and coda waves recorded by the stations in the basin. Cross-correlation functions (c) and dispersion spectrum (d) of 60-second-long ambient noises. The black line in the spectrum graph is fitted dispersion curve of the continuous recording waveforms for one day.

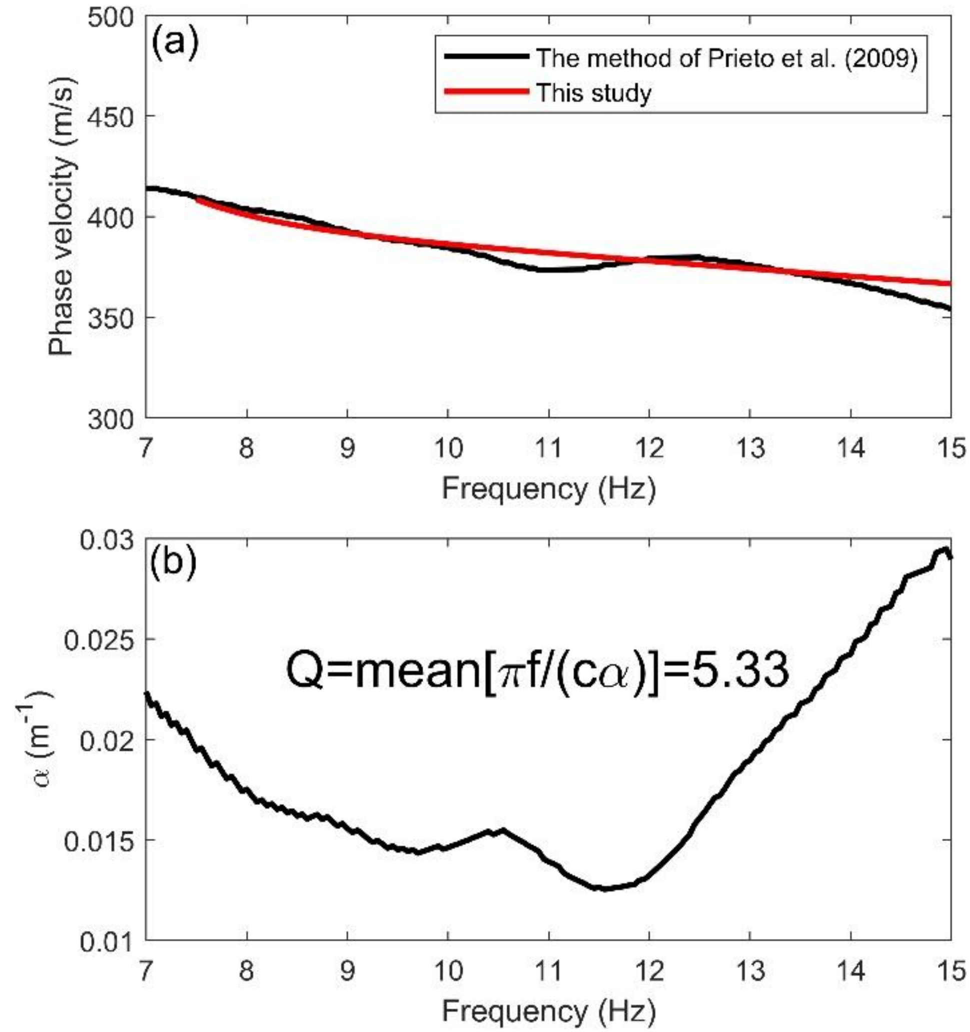

Figure S12. (a) The phase velocity of the classic method introduced by Prieto et al., (2009) and our method. (b) The attenuation coefficient of the classic method. The mean apparent *Q*-value estimated by the classical method is 5.33.